Recent progress in 2D van der Waals heterostructures: fabrication, properties, and applications

Zenghui WANG[1,2*], Bo XU[1], Shenghai PEI[1*], Jiankai ZHU[1], Ting WEN[1],
Chenyin JIAO[1], Jing LI[1], Maodi ZHANG[1] & Juan XIA[1*]

[1]*Institute of Fundamental and Frontier Sciences, University of Electronic Science and Technology of China,
Chengdu 610054, China;*
[2]*State Key Laboratory of Electronic Thin Films and Integrated Devices, University of Electronic Science and
Technology of China, Chengdu 610054, China*

Abstract Two-dimensional van der Waals heterostructures (2D vdW HSs) can be constructed by stacking different 2D materials together in nearly endless ways, and have significantly enriched the 2D materials family. They have attracted intense research attention effort, due to their exotic physical properties and intriguing device performance, often beyond those found in their constituent 2D materials. Here we review research progresses in this emerging 2D system, including fabrication methods, material properties, device applications, and offer our perspectives on emerging research opportunities in this highly active area.

Keywords 2D materials, van der Waals heterostructure, interlayer coupling, stacking, layered nanostructures

1 Introduction

2D materials have been intensively studied for more than a decade [1]. To date, more than a hundred types of 2D materials have been realized with different combinations of elements, including: elementary 2D materials (such as graphene [1] and black phosphorus (bP) [2]); binary-compound 2D materials (such as transition metal dichalcogenides (TMDC) [3], hexagonal boron nitride (h-BN) [4], and CrI_3 family [5]); ternary-compound 2D materials (such as 2D magnets $Cr_2Ge_2Te_6$ (CGT) [6], Fe_3GeTe_2 (FGT) [7], and $MnBi_2Te_4$ (MBT) [8]); and so on.

However, these single crystals only represent a small fraction of 2D materials that have been predicted— many remain yet to be synthesized or grown. This to some extent limits the further exploration of new 2D structures and novel properties, as experimental study always goes after the successful synthesis of a new 2D single crystal. Worldwide, researchers have been devoting tremendous effort to engineering new properties and novel applications in existing 2D single crystals by varying thickness, doping, alloying, intercalation, strain/pressure engineering, etc. Among all the approaches, one method clearly stands out: by simply stacking different 2D materials (two or more) together, one can create 2D vertical van der Waals (vdW) heterostructures (HSs) in nearly endless ways, and thus realize and explore emerging properties in these tailor-made 2D vdW HSs. The investigation of 2D vdW HSs has since been an active research area, creating new opportunities and challenges for researchers in related fields.

Compared to vertical vdW HS, 2D lateral HS is based on the one-to-one bonding within the materials with similar structures and lattice constants, rather than the vdW interaction. Specifically, both 2D lateral HSs and 2D vertical vdW HSs provide new platforms to explore novel physical phenomena, and
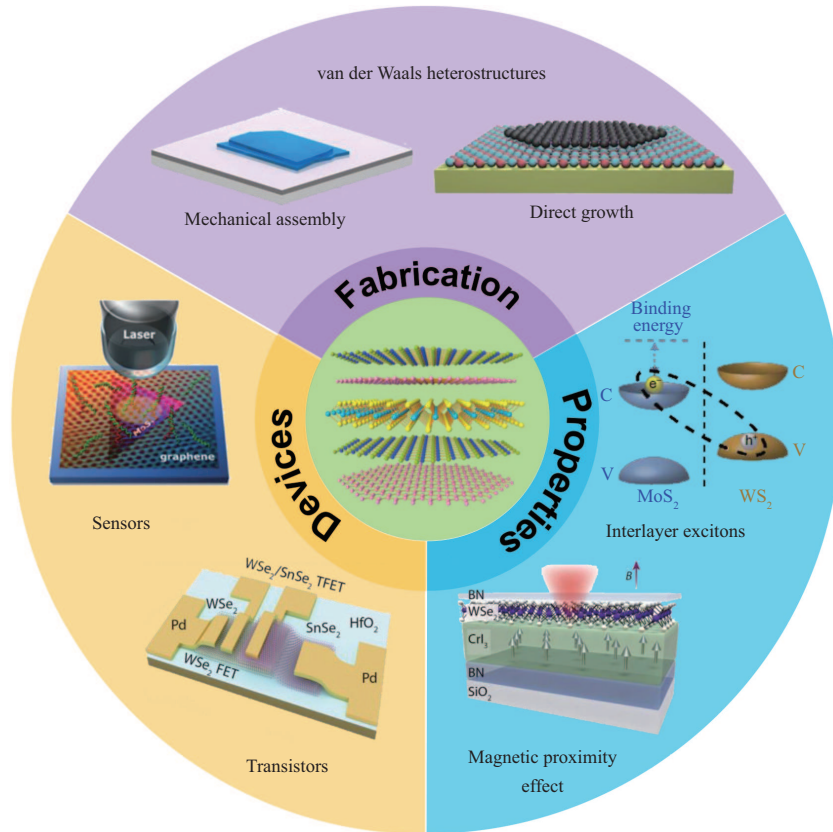
Figure 1 (Color online) Various research thrusts of 2D vdW HSs.

offer new opportunities for enabling next generation 2D devices. In this review, we survey recent progress in fabrication methods, material properties, and device applications of 2D vdW HSs (Figure 1), and offer our perspectives on future research directions.

2 Fabrication

There are various methods to fabricate 2D vdW HSs, which can be categorized into two categories: direct growth and mechanical assembly. Direct growth methods offer an efficient synthesis of new types of 2D HSs with specific twist angles in their most stable phases, typically have high throughput, and produce large-area 2D HS flakes. However, sometimes the grown sample quality could be limited due to the lattice mismatches among different 2D materials. Mechanical assembly methods, in comparison, offer additional degrees of freedom by stacking the pre-grown constituent 2D layers (either by direct growth or mechanical exfoliation) during the assembly process, allowing more structural varieties with the same number of constituent layers. Besides, 2D vdW HSs produced by this method can sometimes avoid the lattice mismatch among 2D layers, and hence possess higher sample quality compared with the direct growth method. Below we survey and compare these fabrication methods in detail.

2.1 Direct growth

Based on different growth techniques, direct growth methods can be categorized into different groups, including chemical vapor deposition (CVD), pulsed laser deposition (PLD) [9], physical vapor deposition (PVD) [10], and molecular beam epitaxy (MBE) [11], etc. Among them, MBE is capable of growing very high-quality samples with minimal impurities and defects, but is limited by stringent growth conditions and prerequisites, high cost, and slow growth rate. PLD has a higher growth rate than MBE, but the growth products also typically have a much higher defect density. CVD and PVD methods strike a nice balance between applicability, growth rate, and sample quality, and are by far the most commonly used techniques for direct growth of 2D HSs, with several representative studies discussed below.

Table 1 Summary of CVD methods for graphene/h-BN vdW HSs

HS structures	Number of growth steps	Growth substrates [Ref.]
Lateral	One-step	Cu foils [12, 14]
	Two-step	Cu foils [16, 17, 19], Ni film [16], Ru(0001) [15], SiO$_2$/Si [18]
Vertical	One-step	Ni film [22]
	Two-step	Cu foil [13, 19, 21], quartz [20]

2.1.1 *Graphene/h-BN HSs*

Graphene is the archetypical 2D material, and its vdW HSs combined with other 2D materials have been grown and studied from more than a decade [12–22]. Due to the same hexagonal symmetry and similar size of carbon and boron/nitrogen atoms, the lattice mismatch between graphene and h-BN is merely about 1.7%, which makes graphene/h-BN one of the most studied 2D HSs. Therefore, the growth of lateral and vertical graphene/h-BN HSs has been explored extensively, as summarized in Table 1.

(1) Lateral graphene/h-BN HSs. Scalable synthesis of lateral 2D HSs is a critical step towards atomically thin two-dimensional integrated circuits. First, choosing a proper substrate is an important prerequisite for the successful growth of 2D HSs.

Copper foil has been serving as the go-to substrate for the growth of graphene/h-BN HSs [13]. Ci et al. [12] directly synthesized lateral graphene/h-BN HSs on Cu substrate by one-step CVD method, using methane and NH$_3$-BH$_3$ as precursors for the growth of graphene and h-BN, respectively. By controlling the ratio of C, B, and N elements, hybridized and randomly distributed domains of h-BN and C phases are obtained (h-BNC), with compositions ranging from pure h-BN to pure graphene. Later, Chang et al. [14] optimized the growth parameter and fabricate graphene/h-BN HSs, including h-BN codoped graphene (h-BNG) (Figure 2(a)).

In addition to copper, ruthenium has also been demonstrated as a suitable substrate to prepare graphene/h-BN HSs [15]. Liu et al. [16] successfully synthesized lateral graphene/h-BN HSs by growing graphene in lithographically patterned h-BN atomic layers, precisely controlling the shapes of graphene and h-BN domains. In addition, other modified CVD methods have also been developed to grow lateral graphene/h-BN HSs, such as epitaxial growth of graphene/h-BN 1D interface [17] and chemical conversion reaction combined with lithography [18].

(2) Vertical graphene/h-BN HSs. 2D vertical HSs have opened up more possibilities in the applications of future photovoltaic, spintronic and excitonic devices, by making use of their unique interlayer degree of freedom. Recent studies show that vertical graphene/h-BN vdW HSs can be synthesized on Cu substrate by two-step CVD methods [13]. Moreover, one can choose whether to form lateral or vertical graphene/h-BN HSs by simply controlling the growth temperature. For example, Gao et al. [19] successfully fabricated lateral and vertical graphene/h-BN HSs by simply choosing the growth temperature of the graphene layer above (lateral) or below (vertical) 900°C. The different growth processes and morphologies of the lateral & vertical graphene/h-BN HSs are shown in Figure 2(b).

In addition, silane- and nickelocene-catalyzed fast growth of graphene/h-BN vertical HSs has been realized [20,21], followed by a one-step CVD growth technique developed for mass production of large-area graphene/h-BN vdW HSs [22]. This technique uses a co-segregation growth process for graphene/h-BN vdW HSs by one-step CVD method [22], in which a sandwich structure (consisting of C-doped nickel top layer, (B, N)-source layer, and Ni bottom layer) is first deposited on a SiO$_2$/Si wafer by electron-beam evaporations. During subsequent vacuum annealing processes, C atoms first segregate from the stack to the surface and form graphene, followed by (B, N) source diffusing and forming an h-BN layer between graphene layer and C-doped Ni layer.

2.1.2 *TMDC/TMDC HSs*

With the clear need for atomically thin semiconducting structures, research interests in heterojunction based on 2D semiconductors (such as TMDC) have been expanding explosively, thus the growth of TMDC/TMDC HSs both in lateral and vertical configurations. Thanks to the similarity in lattice parameters among different TMDCs, many types of TMDC/TMDC HSs have been successfully grown. During growth, a number of factors can be leveraged to control and optimize the growth process of HSs, thus producing either lateral or vertical TMDC/TMDC HSs (see Table 2 [23–39] for a summary).

(1) Precursor/reactants. In 2014, Duan et al. [23] fabricated lateral WS$_2$/WSe$_2$ HSs by a one-step CVD method. To realize the one-step growth of HSs, the system is designed to allow *in-situ* switching of
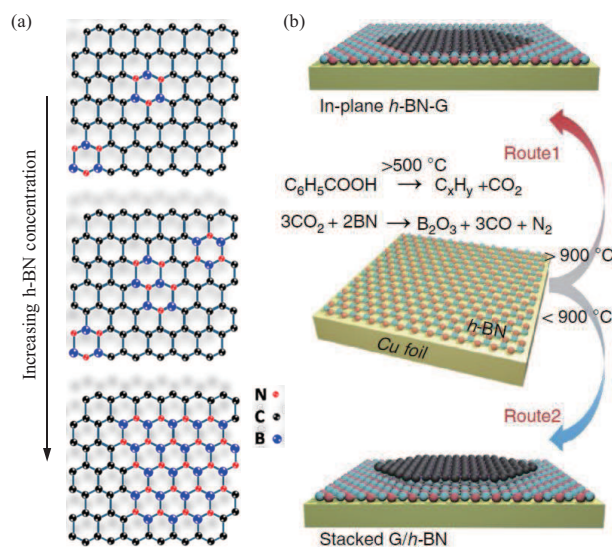
Figure 2 (Color online) (a) Schematic illustration of the structural evolution in h-BNG films with increasing h-BN concentration [14] © 2013 American Chemical Society. (b) Schematic illustration of temperature-triggered switching growth between lateral h-BN/graphene vdW HS (route 1) and vertical graphene/h-BN vdW HS (route 2) [19] © 2015 Springer Nature.

reactants from WS_2 powder to WSe_2 powder. Using similar techniques, lateral and vertical $MoSe_2/WSe_2$ HSs, MoS_2/WS_2 HSs, and WSe_2/SnS_2 HSs are synthesized subsequently [24–28]. In addition, more complicated mixed-phase HSs, such as $MoS_2/Mo_{1-x}W_xS_2$, $Mo_{1-x}W_xS_2/WS_2$, and $WS_2/WS_{2x}Se_{2(1-x)}$ HSs, have also been successfully synthesized [28–30].

(2) Temperature. By controlling growth temperature, Gong et al. [31] designed a one-step CVD method to fabricate both vertical and lateral WS_2/MoS_2 heterobilayers. During the growth process, S powder, MoO_3, and SiO_2/Si with Te+W mixture are placed in a quartz tube in sequence along the direction of gas flow, with the growth temperature set at 850°C for vertical WS_2/MoS_2 HSs, and 650°C for lateral HSs. Temperature controlling is also used to control the TMDC/TMDC vdW HSs growth in a specific sequence, e.g., switching between growing WS_2/MoS_2 vs. MoS_2/WS_2 vdW HSs can be achieved by controlling temperature [32].

(3) Carrier gas. By selecting different carrier gases, one can realize either lateral or vertical TMDC/TMDC HSs in a one-step CVD growth. For example, lateral and vertical WS_2/MoS_2 HSs could be synthesized with and without hydrogen acting as carrier gas [33].

2.1.3 *Superlattice and twisted bilayers*

Compared with the growth of two-component lateral and vertical 2D HSs with one junction, it is more challenging to grow multi-junction superlattices, which have alternating 2D materials repeated with specific periodicities. Some notable achievements have been made, typically by extending the growth steps and addressing the related technical challenges.

Lateral superlattices have been demonstrated through some means. Sahoo et al. [34] reported growth of 2D lateral superlattice with multiple junctions by alternating the growth gas environments. In this method, the N_2+H_2O gas environment is found to facilitate the growth of MoS_2 and $MoSe_2$, while $Ar+H_2$ promotes the growth of WS_2 and WSe_2. Therefore, one can obtain $MoSe_2/WSe_2$ or MoS_2/WS_2 superlattice via repeatedly switching the carrier gas. Besides, one can also grow 2D superlattices by alternating the gas flow direction or varying the types and flow rates of liquid precursors [35–37].

2D vertical superlattices are also realized by several growth methods with more complicated processes. For example, Zhao et al. [38] successfully converted a vertical TMDC HS into a superlattice through a "CVD + mechanical rolling" combing method. As shown in Figure 3, a vertical HS is first synthesized by a typical CVD method, on which a drop of ethanol-water-ammonia solution is applied. As a result of the capillary force, the rolling-up process turns the TMDC vertical HS into a TMDC superlattice. However, the quality of the obtained superlattice could be affected by the residues and impurities from the solution. Recently, a more controllable and cleaner method has been realized to directly grow vertical TMDC superlattices by controlling the flow rate of precursor gas during CVD [39].

Table 2 Summary of CVD methods of TMDC/TMDC vdW HSs

HS structures	Number of growth steps	Growth substrates, if not SiO_2/Si [Ref.]
Lateral	One-step	WS_2/WSe_2 and MoS_2/$MoSe_2$ [23], $MoSe_2$/WSe_2 [24], WS_2/MoS_2 [31], MoS_2/WS_2, MoS_2/$Mo_{1-x}W_xS_2$ and $Mo_{1-x}W_xS_2$/WS_2 [28], WS_2/$WS_{2x}Se_{2(1-x)}$ [29, 30]
	Two-step	MoS_2/WS_2 and $MoSe_2$/WSe_2 [34], TMDC/TMDC [36], WS_2/MoS_2 on sapphire [33]
	Multi-step	TMDC superlattice [35, 37], TMDC superlattice on sapphire [39]
Vertical	One-step	WS_2/MoS_2 [31]
	Two-step	WSe_2/$MoSe_2$ [25], MoS_2/WS_2 [26], WSe_2/SnS_2 [27], WS_2/MoS_2 and MoS_2/WS_2 on Au foil [32], WS_2/MoS_2 on sapphire [33], TMDC superlattice [38]
	Multi-step	TMDC superlattice on sapphire [39]
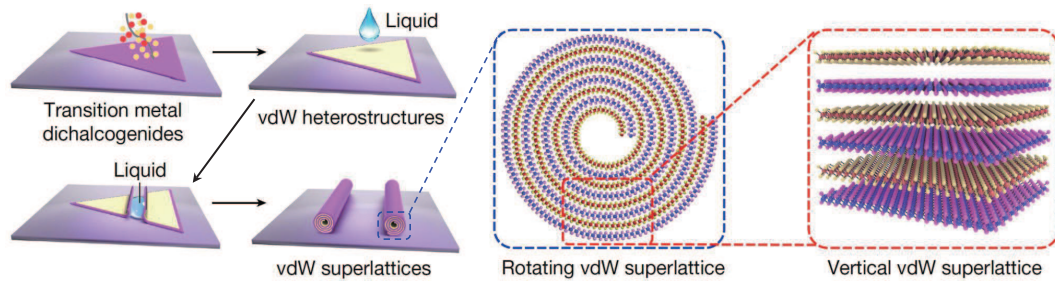
Figure 3 (Color online) Schematic of the synthesis process of the rolled-up vdW HS and the resulting vdW superlattice [38] © 2021 Springer Nature.

Besides controlling the types and numbers of constituent layers in 2D vertical HSs, growing 2D vertical stacks with designated stacking angles is also crucial for realizing tailored properties in these stacked materials. Typically, for 2D twisted bilayers, the most commonly obtained types are those with special angles such as 0°, 30°, and 60°, corresponding to the low-energy configurations. Particularly, twisted bilayer graphene (TBG), MoS_2/MoS_2, and WS_2/WS_2 with random stacking angles have also been reported [40–43], though with low yield and imprecise control of twist angles. Recently, it has been found that gas-flow manipulation could be used to control the twist angle of 2D bilayers, and thus CVD-grown TBG with a wide range of twist angles has been achieved [44].

2.2 Mechanical assembly

The other frequently used method to fabricate 2D vdW HSs is mechanical assembly, which is typically not limited by the lattice mismatch among 2D layers during growth, and hence enables more diverse combinations of different 2D layers, as well as more possibilities of twist angles among layers. The additional degree of freedom offered by this method largely expands the 2D vdW HSs family in a nearly endless way. Below we present several mainstream techniques and examples of fabricating 2D vdW HSs based on mechanical assembly.

2.2.1 *Solution-based transfer*

A solution-based transfer is also referred to as a "wet transfer" technique, which involves several solution-based processes, and typically involves transferring 2D flakes from one substrate to another.

A typical solution-based transfer process using poly (methyl methacrylate) (PMMA) is illustrated in Figure 4(a) [45]. First, PMMA solution is spin-coated and dried on a 2D flakes/SiO_2/Si wafer and forms a PMMA/2D flakes/SiO_2/Si structure, which is then submerged into NaOH aqueous solution to etch SiO_2 layer. After the PMMA/2D flakes film is detached from the previous SiO_2/Si substrate, it is then transferred and precisely aligned to the new substrate, followed by dissolving the PMMA layer with acetone flow. Finally, 2D vdW HSs can be obtained if the target substrate already contains 2D flakes, or by repeating this wet transfer method to stack more 2D layers.

By modifying the above wet transfer method, Dean et al. [46] have obtained cleaner graphene/h-BN HSs without using NaOH aqueous solution (replaced with deionized (DI) water). First, the graphene

flakes are exfoliated onto a polymer stack consisting of a water-soluble layer and PMMA. Next, the water-soluble layer is dissolved away by DI water instead of NaOH solution, leaving the PMMA/graphene film floating. Finally, the PMMA/graphene film is aligned to the target h-BN flake and transferred onto the new substrate using a glass slide, followed by the dissolving of the PMMA. To further reduce solution contamination to the transferred 2D flake, an optimized method has then been developed, by just allowing the water-soluble layer side of the stack to be in contact with water during its dissolving process [47].

2.2.2 *Non-solution-based transfer*

While using solution-based transfer methods, one or more solutions are required to complete the transfer process. This gives rise to the possibility of contamination at the interface between the 2D flakes, which could weaken the interlayer coupling in as-grown 2D vdW HSs. Therefore, non-solution-based transfer methods (often referred to as "dry-transfer" methods) are developed to avoid solution usage and contamination during the construction of 2D vdW HSs.

A typical fabrication process of graphene/h-BN HSs using a dry-transfer method [48] is shown in Figure 4(b). First, a "mask" is prepared, consisting of three layers: glass, tape, and polymer. Next, graphene is deposited on the polymer side of the "mask" by mechanical exfoliation. After the "mask" is flipped with the graphene side facing the substrate, the graphene flake is then aligned and transferred onto the target substrate, which already has an h-BN flake on it. Finally, the whole structure is heated to melt the polymer and thus release the HS from the tape, followed by the dissolving of the remaining polymer with acetone and isopropanol. Note that the polymer dissolving process also involves organic solvent, but it is less likely to contaminate the graphene/h-BN interface since the solvent is applied after the HS is formed.

In another method, two different polymers, polycarbonate (PC) and polydimethylsiloxane (PDMS), are simultaneously used for the creation of more complicated vdW HSs [49]. One example of h-BN/graphene/h-BN fabrication process is illustrated in Figure 4(c). In this method, PDMS serves as a temporary substrate holding one 2D flake, while PC is used to pick up another target 2D flake on the SiO_2/Si wafer. The sample is heated to 60°C–90°C during this process, which ensures that the PC is more adhesive to PDMS than to SiO_2 (so that it does not attach to the substrate) while keeping the 2D materials more adhesive to PC than to SiO_2 (so that they can be picked up). This process can be repeated to form complicated HSs. When it is ready to deposit the HS to a target substrate (which could contain yet another layer of 2D material to add one last layer to the HS), the substrate is heated to 150°C so that the PC layer melts and detaches from the PDMS (together with the HS underneath it). The PC residue covering the HS is then removed by chloroform.

Beyond the above techniques, different combinations of tape, PMMA, polypropylene carbonate (PPC), polyvinyl alcohol (PVA), and PDMS are used for different fabrication purposes of 2D vdW HSs [50, 51]. Temperature is frequently used as a means of controlling the pickup and drop-off processes, as well as improving the interface quality of the HSs [52, 53]. Interestingly, h-BN is found to have stronger adhesion compared with many substrates and polymers, and thus can be used to pick up a selected area/shape of 2D flakes (Figure 4(d)) [50]. This feature of h-BN is highly useful in creating 2D vdW HSs with precise twist angles, which is discussed in Subsection 2.2.3.

Different from the above methods, which still involve the solution process as the last step to remove polymer residue, one completely dry transfer technique has been demonstrated, without any usage of solution throughout the entire transfer, stack, and deposition process [54, 55]. To achieve this, a 2D flake is first exfoliated onto a viscoelastic layer (typically PDMS) by mechanical exfoliation, and then the stamp is aligned to the target substrate and pressed against the substrate with another 2D flake already on it. The stamp is then slowly peeled off, leaving the transferred HS on the target substrate [54]. This technique is particularly useful in creating suspended 2D structures on pre-patterned substrates [55], as any solvent usage during the fabrication process may cause the suspended structure to collapse due to capillary force.

2.2.3 *Tear-and-stack technique*

In recent years, 2D twisted homobilayer systems, such as TBG [56, 57] and twisted TMDC HSs [58, 59], have attracted increasing attention. These bilayer (or even more layer) systems exhibit exotic phenomena like unconventional superconductivity and Moiré potential, which makes the fabrication of these twisted
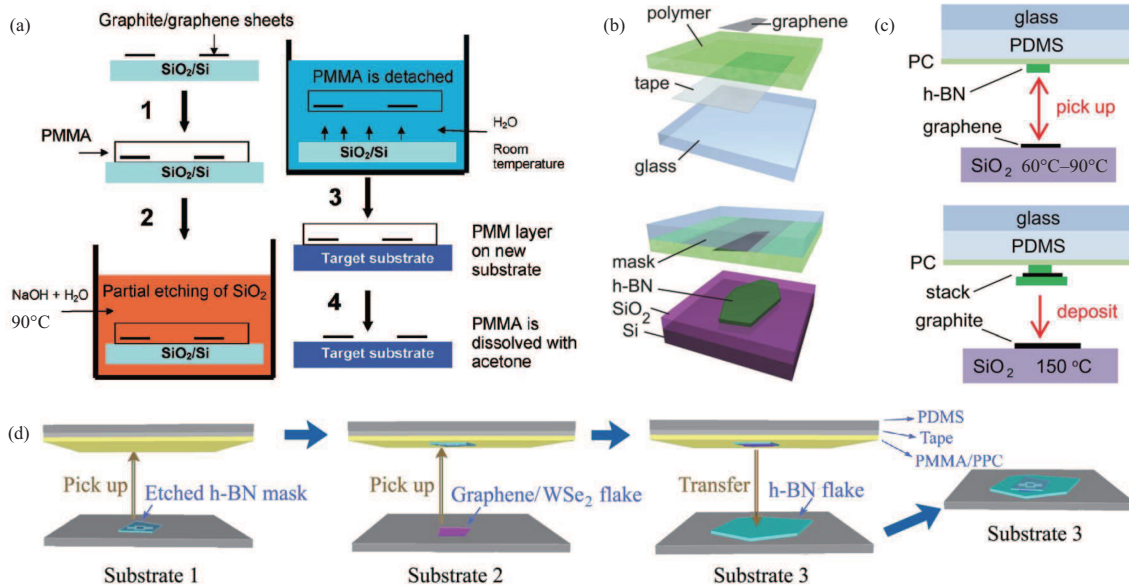
Figure 4 (Color online) (a) Schematic of a wet transfer process. The graphene flakes are first deposited on SiO$_2$/Si substrates via exfoliating highly oriented pyrolytic graphite and are finally transferred onto a nonspecific substrate [45] © 2008 American Chemical Society. (b) Schematic of a typical dry transfer process used to fabricate a graphene/h-BN HS [48] © 2011 American Institute of Physics. (c) Cross section (not to scale) of the glass slide used to pick up a graphene flake. The pick-up process can be repeated several times to create a multilayer HS. In the last step, the stack is released onto graphite on the substrate at an elevated temperature (∼150°C) [49] © 2014 American Institute of Physics. (d) Schematic of pick-up technique for fabrication of encapsulated devices with the h-BN mask on top [50] © 2015 American Chemical Society.

homobilayer structures with controlled twist angle an important subject. Among all the fabrication methods, the tear-and-stack technique is the most commonly used one to achieve such twisted homobilayers. This technique could be summarized as a two-step process: first, selectively pick up (tear) one part of a 2D flake, and next, stack it onto the other part of the same flake. Generally speaking, in the step when the twisted bilayer is created, no solution is involved; though it could be used at the end when the polymer is dissolved if any.

One example of this tear-and-stack technique to fabricate TBG is shown in Figure 5(a). First, a femtosecond laser is used to complete the "tear" process, with a monolayer graphene flake being cut into many pieces with straight edges. Then, by stacking them with a dry-transfer method with the straight edges used to determine the twist angles, TBG flakes with controllable twist angles are obtained [60]. Another example could be found in Figure 5(b), which instead uses an AFM tip to scribe through a 2D flake in contact mode, thus partially cutting the sheet and then folding it into a homobilayer [61].

A more broadly used tear-and-stack strategy [62] is to use h-BN to tear the 2D flake apart, leveraging the strong adhesion between h-BN and other 2D materials. A typical process of TBG fabrication using this technique is illustrated in Figure 5(c). First, a hemispherical handle with PVA-coated epoxy picks up an h-BN flake, which is then used to adhere and tear apart the target graphene flake on the SiO$_2$/Si substrate. Given the difference in adhesion strength between h-BN/graphene and h-BN/SiO$_2$ surfaces, only the graphene part in direct contact with h-BN will be picked up, leaving the other part on the substrate. Then, the handle is rotated at a given angle to the substrate before picking up the remaining part of the graphene flake. Finally, the TBG stack is then deposited into a new substrate, with polymer removed as in other transfer techniques mentioned above.

All the above techniques have played important roles in 2D HS research. While a solution-based transfer method has been quite successfully used in many experiments, non-solution-based transfer methods have become more popular due to the advantage of creating clean interfaces. Meanwhile, more types of polymers have been introduced in transferring 2D materials. For example, PDMS, PPC, PC, and polyethylene terephthalate (PET) have been used to create 2D vdW HSs. In addition, the "tear-and-stack" method is also becoming increasingly important with the rise of Moiré superlattices, thanks to its capability of producing bilayer systems with well-defined twist angles.
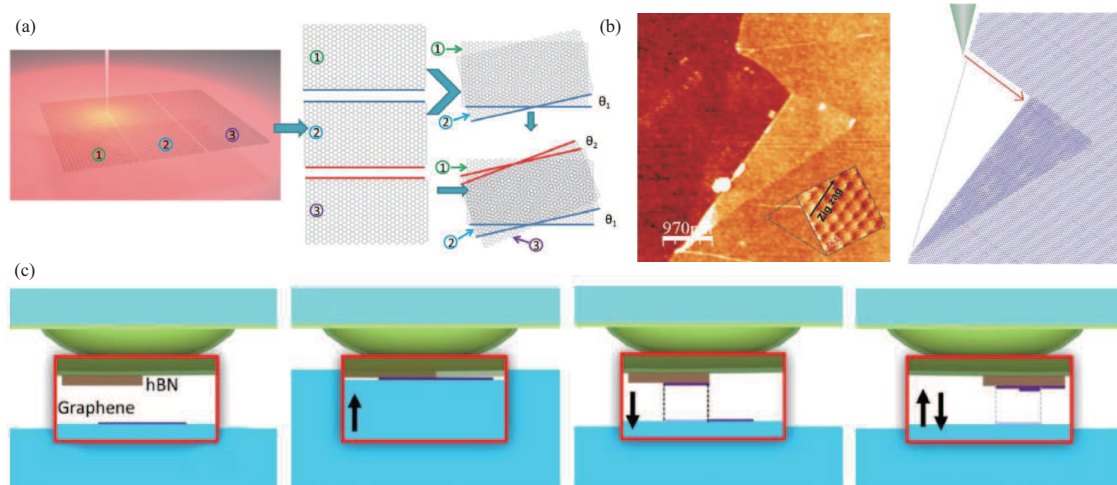
Figure 5 (Color online) (a) Schematic of a cutting-rotation-stacking technique used to fabricate TBG and double twisted trilayer graphene [60] © 2016 John Wiley & Sons. (b) AFM image of a folded graphene. The inset shows a high-resolution AFM image that determines the zigzag crystallographic orientation of the bottom layer (left). Schematics of the folding procedure, notice that a Moiré pattern is generated in the folded region (right) [61] © 2011 American Chemical Society. (c) Rotationally aligned graphene double-layer realized by successive transfers from a piece of monolayer graphene using a hemispherical handle substrate, and the red box represents a zoom-in view of the hemispherical handle substrate. From left to right: before pick-up; partial contact of the h-BN with the bottom graphene; raising the h-BN tearing one section of graphene; the second pick-up to create an overlap region of the two graphene layers [62] © 2016 American Chemical Society.

3 Material properties

Not only do 2D HS systems inherit the properties of their constituent 2D layers, but they also offer new degrees of freedom by combing different 2D materials in endless ways. Therefore, 2D HSs are excellent platforms for exploring and investigating exquisite physical phenomena, such as magnetic proximity effect (MPE), interlayer excitons, superconductivity, and ferroelectricity. Below we survey and discuss a few examples of the optical, magnetic, and electrical properties of 2D HSs.

3.1 Optical properties

Optical characterization of 2D vdW HSs usually includes photoluminescence (PL), Raman scattering, and absorption [63, 64]. Through tracking and analyzing the spectral features in 2D vdW HSs, properties related to their interlayer coupling and band structure can be studied. The optical properties of these vdW HSs could be sensitively tuned by both intrinsic parameters (such as material composition) and external fields (such as pressure). Here we discuss the interlayer excitons and Raman behaviors in several representative vdW HSs.

3.1.1 *Interlayer excitons*

Excitons are electron-hole pairs bound by Coulomb interaction in semiconductors. Typically, the binding energy of excitons can be extracted from the PL or absorption spectra of the sample. With reduced dielectric screening, 2D materials have larger exciton binding energy (compared with those in 3D crystals) and hence more prominent excitonic behaviors. Moreover, different from excitons in monolayer and bulk 2D materials, 2D vdW HSs have the unique concept of interlayer exciton vs. intralayer exciton. These two types of excitons have different physical origins and show distinct tunability to external fields.

The study of interlayer excitons is of great importance for understanding the physical mechanism of interlayer coupling in 2D HSs. One prerequisite for a 2D heterobilayer structure to form interlayer excitons is that it has type-II band alignment, as shown in Figure 6(a) [64]. Typically, a type-II vdW HS with moderate interlayer coupling could be excited to exhibit both intralayer and interlayer excitonic emissions (the top panel of Figure 6(a)), while the HSs with very weak interlayer coupling may only have intralayer excitonic emissions from the individual layers (the bottom panel of Figure 6(a)).

There are several ways known to enhance interlayer coupling in 2D HSs, making precise investigation of interlayer excitons possible. Mainstream approaches include epitaxial growth to directly obtain 2D HSs with a clean interface [64], annealing to reduce the interlayer distance of as-transferred 2D HSs [65],
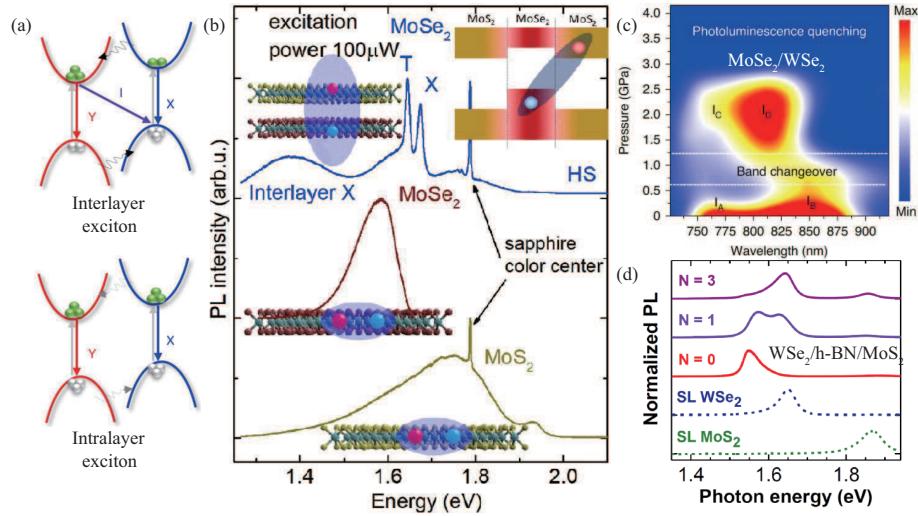
Figure 6 (Color online) (a) Simplified schematic illustration of excitation, charge separation and emission processes in type-II-alignment 2D HSs with moderate (top) and weak (bottom) interlayer coupling; only the top case possesses interlayer excitons [64] © 2021 Springer Nature. (b) Normalized PL spectra at 10 K of $MoSe_2/MoS_2$ heterobilayer, and as-grown $MoSe_2$ and MoS_2 single layers. $MoSe_2/MoS_2$ HS exhibits both intralayer and interlayer excitons [67] © 2017 American Chemical Society. (c) Evolution of the PL spectrum with pressure in a color plot for the $WSe_2/MoSe_2$ HS [64] © 2021 Springer Nature. (d) Normalized PL spectra of single-layer WSe_2, MoS_2, and WSe_2/MoS_2 heterobilayer with n layers of inserted h-BN ($N = 0$, 1, and 3) [82] © 2014 National Academy of Sciences.

and focused-laser treatment to enhance interlayer coupling for 2D HSs [66]. Figure 6(b) [67] shows an example of 2D vdW HS ($MoSe_2/MoS_2$) with moderate interlayer coupling, thus exhibiting PL emissions from both intralayer and interlayer excitons.

Tunable interlayer excitons. As mentioned above, interlayer excitons show greater sensitivity (and thus tunability) to external fields than intralayer ones, especially in terms of emission energy and exciton lifetime [68,69]. Some of the typical tuning methods include gating [68,70–73], temperature [74], excitation power [74,75], twist angle [69,76–78], magnetic field [79], and strain [80]. For example, using electrostatic gating, Rivera et al. [68] studied a $WSe_2/MoSe_2$ HS and found both the energy (blue shifts by ∼45 meV) and intensity of its interlayer excitons are highly tunable with applied gate voltage, which is scanned from +100 to −100 V. This is attributed to the coupling between the applied electrical field and the anti-aligned dipole of the interlayer exciton. This study also finds that the lifetime of the interlayer exciton is an order of magnitude longer than intralayer excitons. In addition, exciton lifetime in $MoSe_2/WSe_2$ HSs is highly sensitive to temperature and twist-angle [69].

Pressure engineering is known as a highly effective, reversible, and *in-situ* technique for modulating the interlayer excitonic behavior of 2D vdW HSs by controlling the interlayer distance. For example, calculations show that MoS_2/WS_2 HS could be transformed from an indirect-gap semiconductor to a direct-gap one by changing the interlayer distance [81]. Experimentally, Xia et al. [64] studied a $WSe_2/MoSe_2$ HS sample and demonstrated efficient tuning of its interlayer coupling by pressure engineering, observing a pressure-induced band changeover as shown in Figure 6(c).

Reversely, one can also increase the interlayer distance of a 2D HS by inserting dielectric layers (e.g., h-BN) into the vdW gap, and thus effectively tune the interlayer coupling and excitonic behaviors in 2D HSs. One example of this interlayer-distance-increasing method (using WSe_2/MoS_2 HSs as samples) is illustrated in Figure 6(d) [82], where the emission energy of interlayer excitons is modulated by the inserted h-BN layers with different thicknesses.

Moiré excitons. Moiré superlattices in 2D vdW systems provide an attractive platform to study the emerging physics in these periodic structures, offering intriguing opportunities to engineer the band structure of collective excitations. For example, the Moiré excitons in WSe_2/WS_2 HSs with small twist angles exhibit gate dependences, different than the A exciton in WSe_2 monolayers and WSe_2/WS_2 HSs with large twist angles [83]. Liu et al. [59] reported optical signatures of trions coupled to the Moiré potential in bilayer $WSe_2/MoSe_2$ HSs: the Moiré trions show multiple sharp emission lines, in contrast to the behavior of conventional trions without Moiré potential. Besides, the interaction and coupling between Moiré excitons and photons in 2D HSs have been studied: for example, a distributed Bragg
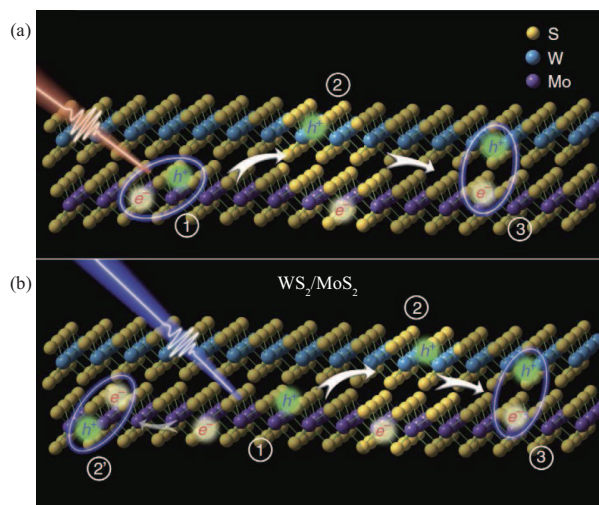
Figure 7   (Color online) (a), (b) Illustrations of the light-induced charge separation and the formation of interlayer exciton in a WS$_2$/MoS$_2$ HS: ① immediately after photoexcitation, electron/hole pairs, intralayer excitons, and other carriers are generated in each layer, ② holes transfer to WS$_2$ and electrons transfer to MoS$_2$ to form the intermediate states (interlayer hot excitons), ③ the hot excitons relax to generate the tightly bound interlayer excitons [89] © 2016 Springer Nature.

reflector consisting of MoSe$_2$/WS$_2$ HSs exhibits cooperative coupling between Moiré-lattice excitons and microcavity photons [84].

Exciton dynamics: ultrafast charge transfer. The ultrafast charge transfer processes in 2D vdW HSs have been widely studied, which embeds rich information of both intralayer and interlayer exciton dynamics. In particular, 2D HSs with strong interlayer coupling promote the charge transfer between two layers, which further affects the exciton recombination process within the individual layers [66]. Hong et al. [85] reported the first experimental observation of ultrafast charge transfer (50 fs) in photoexcited MoS$_2$/WS$_2$ HSs and suggested that the proximity of the two monolayers contributes to the ultrafast charge transfer process.

Similarly, ultrafast charge transfer processes have been found in graphene (or graphite)/TMDC HSs (400 fs∼1 ps) [86, 87] and MoS$_2$/WSe$_2$ HS (470 fs) [88]. Chen et al. [89] experimentally analyzed the transfer process in an MoS$_2$/WS$_2$ HS by ultrafast visible/IR microspectroscopy, as shown in Figures 7(a) and (b). This study demonstrates that the ultrafast charge transfer between the WS$_2$ and MoS$_2$ monolayers results in an intermediate state of electron/hole pair with excess energy, before the formation of tightly bound interlayer excitons after an interlayer charge-transfer process.

3.1.2   *Raman scattering*

Raman spectroscopy can reveal rich structural information in 2D vdW HSs, such as structure instability, interlayer distance, interlayer sliding, and phase transition. Specifically, ultra-low frequency Raman spectroscopy enables precise measurement of interlayer vibration (and thus interlayer interaction) in vdW HSs, therefore allowing identification of the twist angles in these 2D HSs [64, 90].

For example, Quan et al. [90] studied the phonon renormalization in MoS$_2$/MoS$_2$ Moiré HSs, and discovered that the interlayer phonon modes shift rapidly with twist angle. This is due to the ultra-strong coupling between different phonon modes and the atomic reconstructions of the Moiré pattern, which exist over a range of small twist angles. Besides, the relationship between Davydov splitting of the high-frequency intralayer vibrations and the low-frequency interlayer vibrations in twisted multilayer MoTe$_2$ is also experimentally studied, where the out-of-plane intralayer modes are found to be more sensitive to the interfacial layer-breathing coupling [91].

3.2   **Magnetic properties**

Since the discovery of intrinsic 2D magnetism in monolayer CrI$_3$ [5] and bilayer CGT [6] in 2017, 2D magnetic materials and their vdW HSs have attracted tremendous attention. In this emerging field, the study of magnetic vdW HSs, including theoretical explorations, mainly focuses on 2D HSs stacked with monolayer TMDC and 2D magnets [92–94].

On the one hand, the TMDC layer affects the magnetic properties of 2D magnets. Taking WSe_2/CrI_3 HSs as an example: it is predicted that after forming WSe_2/CrI_3 HSs, monolayer CrI_3 undergoes a direct to indirect band gap transition, and easy magnetization direction changes from out-of-plane to in-plane [92], with the generation of topologically nontrivial states [93].

On the other hand, owing to the intrinsic magnetism of the 2D magnets, the physical properties of the TMDC layer in HSs can also be tuned. Figure 8(a) shows that the PL intensity of WS_2 is largely enhanced after forming WS_2/CGT HSs [95]. In addition, other intriguing phenomena have also been predicted or found in TMDC/2D magnet HSs, such as MPE induced Zeeman splitting [96,97], exchange bias and spin-wave dynamics [98], and the formation of 2D-magnet-based magnetic tunneling junctions (MTJs). These exotic optical and magnetic properties in 2D HSs dominated by interlayer interaction will be discussed in detail below.

3.2.1 *Magnetic proximity effect*

Magnetic proximity effect (MPE) is a type of interfacial effect in vdW HSs consisting of 2D magnets and other 2D materials. Using WSe_2/CrX_3 (X = I, Br, or Cl) HSs as an example, MPE refers to the magnetic effect on the WSe_2 layer induced by the adjacent magnetic CrX_3 layer [96,97]. To date, Zeeman splitting is the most studied MPE in TMDC/CrX_3, graphene/CrX_3, and HSs consisting of two different 2D magnets.

Valley Zeeman splitting. Owing to the unique valley nature of TMDC, valley Zeeman splitting is prominent in TMDC/CrX_3 HSs, and thus has been studied intensively.

(1) Valley splitting characterized by the magneto-PL method. Thanks to the excellent PL property of monolayer WSe_2 and the strong magnetic field of CrI_3, the WSe_2/CrI_3 system provides an ideal platform for studying the magneto-PL effect, revealing clear valley splitting [97,99] and charge transfer processes in such HSs [97,100]. For example, in WSe_2/CrI_3 HS, rapid switching of valley splitting and polarization in monolayer WSe_2 are demonstrated via magnetization flipping in the CrI_3 layer [99], as shown in Figures 8(b)–(d). In $MoSe_2/CrBr_3$ HSs, the valley polarization of the $MoSe_2$ trion state is strongly affected by the local $CrBr_3$ magnetization, while the neutral exciton state remains insensitive [101].

(2) Valley splitting modulated by an external field. Through the MPE, laser power can be used to continuously and efficiently tune the valley polarization and valley Zeeman splitting in WSe_2/CrI_3 HS [102]. Figure 8(e) shows the modulation of valley polarization and splitting via optical excitation power in a WSe_2/CrI_3 HS, which suggests an efficient pathway to optically tune the magnetic exchange field in 2D HSs. In addition, it is expected or shown that valley splitting can also be tuned by intrinsic point defects [103], twist angle [96], strain [104], pressure [105], and gating [96,106]. Figures 8(f) and (g) show gate modulation of valley splitting in an $MoSe_2/CrBr_3$ HS measured by reflection spectroscopy [107], revealing electric field dependences of the MPE and the tunneling rate across the $MoSe_2/CrBr_3$ interface.

(3) The physical nature of valley splitting. The origin of the large valley splitting phenomenon in WSe_2/CrI_3 HSs has been widely studied. It has been proposed that the distinct exchange interactions between spin and pseudospin due to W-Cr superposition are responsible for the splitting [108,109]. Theoretically, Hu et al. [110] discover a valley splitting in WSe_2/CrI_3 HSs based on the coexistence of inversion and time-reversal symmetry breaking, and suggest that the valley splitting is a robust feature regardless of the CrI_3 thickness.

Zeeman splitting and Zeeman spin Hall effect. Besides monolayer TMDC, graphene is also found to exhibit strong MPE when forming an HS with CrX_3, which includes Zeeman splitting and Zeeman spin Hall effect [111–113]. For example, clear Zeeman splitting in 2L-graphene/$CrCl_3$ HS has been observed (Figures 8(h) and (i)), in which the enhancement of the nonlocal signal near the Dirac point mainly originates from the exchange-field-induced Zeeman spin Hall effect [113]. Zeeman splitting is also found in graphene/$CrBr_3$ HSs [112], and the MPE in these 2D HSs is expected to be modulated by pressure [114] and electric field [115].

3.2.2 *Exchange bias*

The interaction between different 2D magnets can give rise to some intriguing phenomena in HSs consisting of two different 2D magnets, such as enhanced ferromagnetic properties of FGT in $FePS_3/FGT$ HSs [116], elevated Curie temperature in VI_3/CrI_3 and $FePS_3/FGT$ HSs (compared with individual 2D magnets) [105,116], spin-Seebeck effect in $CrI_3/NiCl_2$ HSs [117], and electrical-field-tuned quantum anomalous Hall effect in $MnBi_2Te_4/CrI_3$ HSs [118].
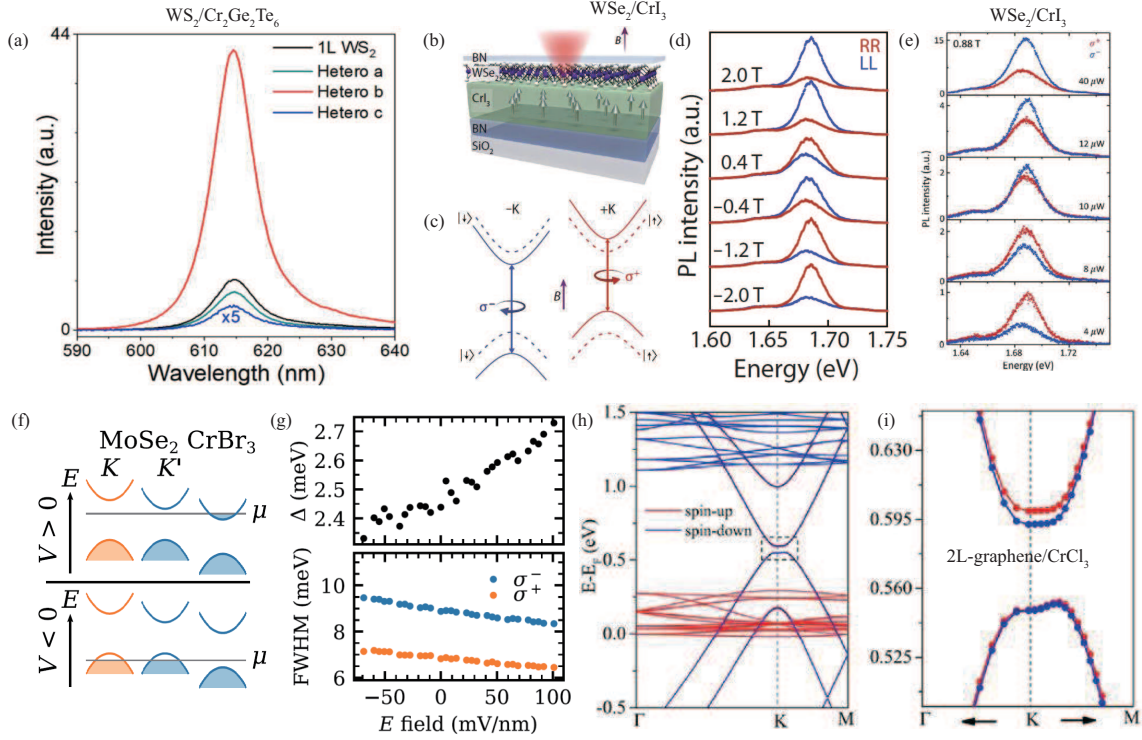
Figure 8 (Color online) (a) PL spectra of 1L-WS$_2$ and HSs with different-thickness CGT. 1L-WS$_2$/6L-CGT exhibits a strong enhancement of PL intensity [95] © 2021 American Chemical Society. (b) Schematic of an h-BN/1L-WSe$_2$/CrI$_3$/h-BN vdW HS [99] © 2017 The Authors. (c) Spin-valley locking effect and valley-dependent optical selection rules in monolayer WSe$_2$, dashed (solid) lines indicate the band edges before (after) exchange field coupling [99] © 2017 The Authors. (d) Circularly polarized PL spectra under different magnetic fields, exhibiting clear valley Zeeman splitting [99] © 2017 The Authors. (e) Laser power modulation of valley polarization and splitting in 1L-WSe$_2$/CrI$_3$ HS [102] © 2018 American Chemical Society. (f) Schematic of the type-II band alignment of MoSe$_2$ and CrBr$_3$ with chemical potential μ for positive and negative gate voltages [107] © 2020 American Physical Society. (g) Out-of-plane electric field dependence of the valley splitting Δ and FWHM of the exciton peaks in MoSe$_2$/CrBr$_3$ HS [107] © 2020 American Physical Society. (h) Band structure of 2L-graphene/CrCl$_3$ HS [113] © 2021 American Chemical Society. (i) Zoom-in of the dashed box in (h), showing Zeeman splitting effect [113] © 2021 American Chemical Society.

Among the many physical processes, exchange bias is the most widely studied in such 2D magnets HSs. It refers to the magnetic coupling phenomenon in which the spins in a ferromagnet (FM) are pinned by those of an antiferromagnet (AFM) [118, 119]. Exchange bias is related to the exchange coupling between an FM and an AFM [120], and can be influenced by the non-nearest neighbor magnetic layer (and thus depends on the thickness of the 2D magnetic layers). This is different than MPE, which is entirely interfacial (and thus independent of the thickness of 2D magnets). Figure 9(a) shows an example of the exchange-bias fields in CrCl$_3$/FGT HSs tuned by the field-cooling process and the thickness of CrCl$_3$ [119].

3.2.3 *MTJs*

MTJs refer to a type of 2D HSs consisting of both 2D magnets and a non-magnetic tunneling layer. The large tunneling magnetoresistance (TMR) found in MTJs makes this kind of material promising for novel devices such as spin-torque diodes, high frequency oscillators, and magnetic random access memory devices. The two most-studied categories of 2D-HS-based MTJs are the nonmagnetic (NM) layer sandwiched by magnetic (M) layers (M/NM/M) and the M layer sandwiched by NM layers (NM/M/NM), which we discuss below.

M/NM/M MTJ systems. An M/NM/M MTJ system is composed of an NM layer sandwiched by two M layers. To date, large TMR effect has been predicted in CrX$_3$/h-BN/CrX$_3$ (X = Br, I) [121], FGT/h-BN/FGT [122,123], VSe$_2$/h-BN/VSe$_2$ [124], and MnSe$_2$/h-BN/MnSe$_2$ MTJs [124], all with h-BN serving as the tunneling layer. These studies reveal that the TMR effect in 2D-based MTJs is sensitive to the thickness of the M layer [125].

In addition to h-BN, TMDCs can also be sandwiched between the M layer and make MTJ systems [126,127]. Figure 9(b) shows the magnetoresistance of an FGT/MoS$_2$/FGT MTJ at 1 μA bias
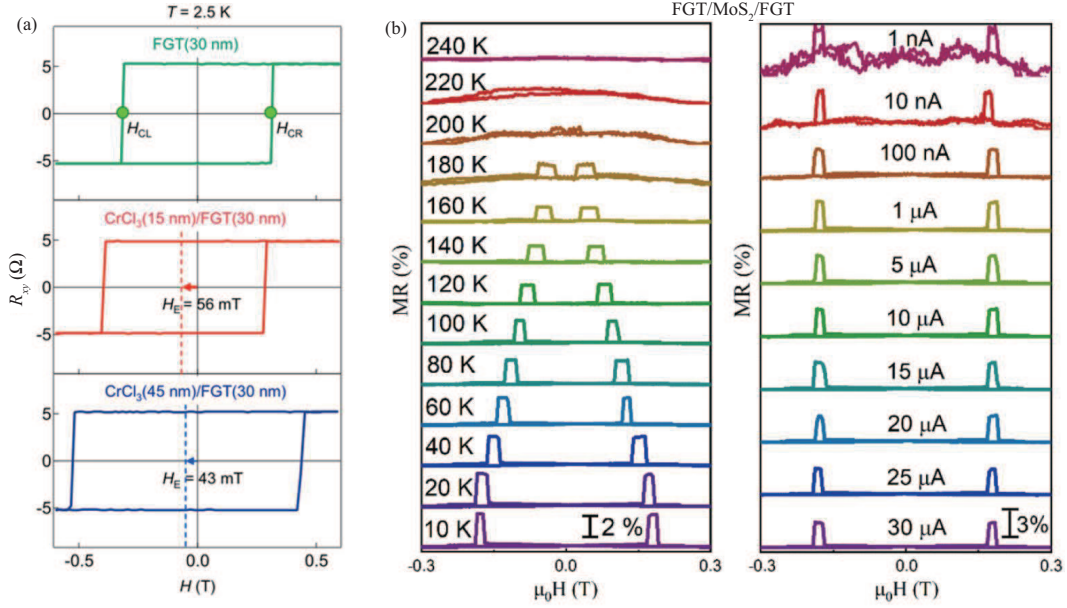
Figure 9 (Color online) (a) $R_{xy} \sim H$ hysteresis loops for FGT and two different CrCl$_3$/FGT HSs measured at 2.5 K [119] © 2020 American Chemical Society. (b) Magnetoresistance of an FGT/MoS$_2$/FGT MTJ measured under different temperatures in the range of 10–240 K with a constant bias current of 1 μA, and measured at 10 K under different bias currents from 1 nA to 30 μA [126] © 2020 American Chemical Society.

current under different temperatures (10~240 K), and under different bias current (1 nA to 30 μA) at 10 K. In this MTJ, MoS$_2$ serves as a conducting layer, and the TMR of junction increases monotonically as temperature or bias current decrease [126].

NM/M/NM MTJ systems. An NM/M/NM MTJ system, in contrast, consists of an M layer sandwiched by two NM layers. For example, an h-BN/graphite/CrI$_3$/graphite/h-BN tetralayer junction [128] has been demonstrated, with two graphite sheets serving as electrodes. The tunneling conductance of CrI$_3$ is measured as a function of temperature and applied magnetic field, revealing a field induced metamagnetic transition with large TMR (95% in bilayer CrI$_3$ device). Besides such a large TMR effect [129, 130], other phenomena have also been observed or predicted, such as enhancement of interlayer magnetic coupling by hydrostatic pressure in h-BN/graphene/CrI$_3$/graphene/h-BN HS [131], chiral edge state in a lateral WTe$_2$/CrI$_3$/WTe$_2$ junction [132], and spin transport in graphene/CrI$_3$/graphene MTJs [133].

3.3 Electrical properties

Electrical properties of vdW HSs have been intensively studied and have important implications for potential device applications. Meanwhile, from a fundamental science perspective, electrical transport measurements can also reveal important physical processes. The unique electronic properties of vdW HSs mainly come from two facts: device structure and electronic structure, which we briefly survey below.

3.3.1 *Device structure*

The additional stacking degree of freedom offered by vdW HSs allows the device structures to be further optimized, leading to intriguing electronic performance. The main advantages of using vdW HSs typically come from the improved substrate surface, better electric contact, and enhanced gating efficiency.

(1) Substrate surface. 2D vdW HS structure allows researchers to effectively change the substrate experienced by the channel layer in an electronic device, and the most commonly used "substrate" material is h-BN. Dean et al. [46] measured transport characteristics of graphene/h-BN HSs in comparison to graphene devices on the SiO$_2$/Si substrate, and showed that h-BN constitutes a much better substrate with an atomically smooth surface. Consequently, graphene devices on h-BN substrates exhibit almost an order of magnitude higher mobility than devices on SiO$_2$. Such high mobility in graphene/h-BN HSs can also be obtained using a dry-transfer method, which is almost completely free of bubbles or wrinkles [48].

Inspired by the intriguing results of using HS device structure to effectively improve the device substrate, which is in contact with the channel material on the bottom side, researchers went further to encapsulate the channel material on both sides, forming a sandwich structure. For example, h-BN/WSe$_2$/h-BN HSs have been demonstrated with excellent electrical properties [50]. These results show that vdW HSs allow efficient control of the surface smoothness and dielectric environment experienced by the channel layer, and can thus effectively improve the devices' electronic properties.

(2) Electric contact. HS device structure can also be used to improve electrical contacts. For example, electrical transport properties of h-BN/bP/h-BN HSs [134] have been investigated and compared with non-HS devices using Co/bP contacts. Researchers find that the Co/h-BN contacted bP transistors in the HS show n-type characteristics with significantly decreased work function, a clear improvement from the non-HS Co/bP contacts. In addition to carrier injection, HS device structures are also expected to improve the efficiency of spin injection: calculation shows that Ni(111)/h-BN/graphene HSs exhibit high spin-injection efficiency with the presence of an h-BN barrier [135].

(3) Gating efficiency. The HS device structure also facilitates the implementation of novel device structures with atomically thin gate dielectric layers to improve gating efficiency in electronic devices. One of the most commonly used gate dielectrics is h-BN [136], and in vdW HSs this allows the gate (often made of graphene) to be positioned much closer to the channel (down to a few nm), and thus much higher gating efficiencies be achieved than in devices gated through conventional SiO$_2$ dielectric (typically hundreds of nm thick).

In addition, researchers have also used the sandwich structure to create vdW HSs with atomically thin gate dielectric on both sides, in order to fully control the out-of-plane electric field through the channel layer. For example, Fei et al. [137] fabricated graphene/h-BN/WTe$_2$/h-BN/graphene HSs and studied the electric polarization of WTe$_2$ using the combination of top and bottom graphene gates (and the h-BN layers serving as gate dielectric). Such HS structure allows researchers to study spontaneous out-of-plane electric polarization in the WTe$_2$ layer and realize ferroelectric switching in such atomically thin vdW HSs.

3.3.2 *Electronic structure*

While the electronic properties of the vdW HSs can be enhanced through improvements in the substrate surface, electric contact, and gating efficiency, the channel layer where electric transport takes place can also be engineered using the additional stacking degree of freedom, giving rise to new electronic structures and thus exotic transport properties. One of the most intensely studied examples is twisted bilayer HS (in particular bilayer graphene) [56, 57, 138–140], in which researchers tune the electronic structure of bilayer HSs through interlayer interactions by varying the twist angles.

Early theoretical study [138] showed that the low energy dispersion is linear in small-angle TBG, and an external electric field cannot open an electronic gap. Surprisingly, Cao et al. [139] observed and demonstrated insulating states in h-BN/TBG/h-BN HSs with small angles induced by strong interlayer interactions (Figure 10(a)). Later, the same group of researchers found that as the twist angle in TBG reaches 1.1° (the so-called "magic angle"), the band structure near zero Fermi energy becomes flat owing to strong interlayer coupling [56, 57], and tunable zero-resistance states with a critical temperature of up to 1.7 kelvin can be observed. Electronic properties of TBG with twist angles smaller than 1° have also been investigated [140] and are found to be strongly altered by electron-electron interactions (Figure 10(b)).

In addition to TBG HSs, twisted bilayer h-BN/h-BN HSs [141] have also been studied, which exhibit ferroelectricity even at room temperature. These examples show that the stacking degree of freedom in vdW HSs offers great opportunities for researchers to explore all kinds of device structures, and take advantage of the interlayer interaction to realize novel electronic devices. More complicated HS device structures, such as those involving both graphene and TMDC, have also been extensively studied, which we will survey in the section "FET devices".

It is important to note that optical, magnetic, and electrical properties are not completely independent, and the modulations of different properties are not mutually exclusive. Specifically, when subjecting HSs to external modulations, such as doping, laser pumping, and pressure engineering, many different physical properties could change at the same time. Similarly, individual characterization techniques can be used to study different properties. For example, PL spectra can be used to monitor electronic band evolution, and circularly polarized PL spectra can be used to observe valley Zeeman splitting due to changes in magnetic
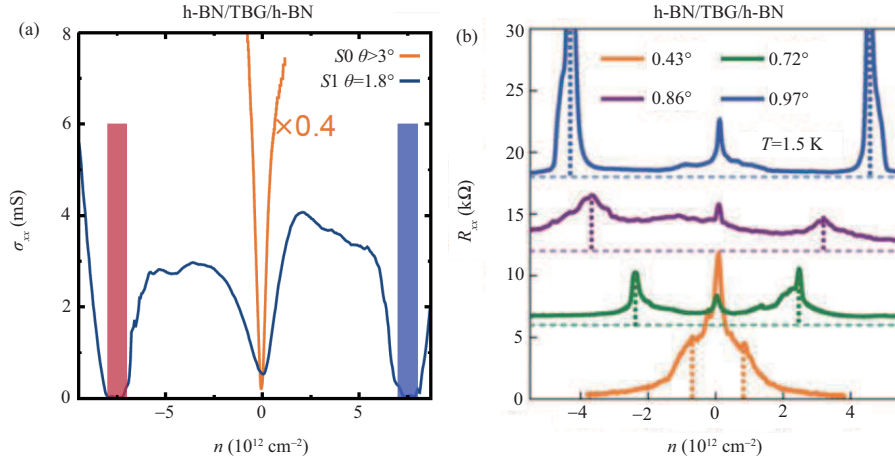
Figure 10 (Color online) (a) Comparison of the conductivity of a large-angle and a small-angle TBG device. The vertical bars around $n = \pm 7.5 \times 10^{12}$ cm^{-2} indicate the insulating states [139] © 2016 American Physical Society. (b) R_{xx} vs. n measured at $T = 1.5$ K in small-angles TBG with different twist angles [140] © 2017 National Academy of Sciences.

moments. Therefore, it is important to have different characterizing techniques, allowing researchers to comprehensively study the various physical properties within 2D HSs.

4 Device applications

The intriguing material properties discussed above make these 2D vdW HSs [142] of great promise for creating atomically thin devices [143–146], such as field-effect transistors (FETs), photovoltaic devices, sensors, memory devices, and mechanical resonators. In addition, one can realize multifunctional vdW HS-based devices by leveraging different properties within the same structure [147–157]: for example, MoS_2/h-BN/graphene HS can serve as both random access memory [158] and photodetector [159]; with proper design, it is entirely possible that these different functions can be integrated within the same device, and enable new designs such as light-sensitive imaging arrays with memory functions. For example, an ReS_2/h-BN/graphene HS can be used to realize a tunneling diode, a logic gate, an FET, and a memory device [152]; an $MoTe_2$/MoS_2 HS can be designed for a device acting as a self-powered photodetector and a ternary inverter [154]; an MoS_2/WSe_2/MoS_2 HS can potentially function as an FET, a biosensor and a PH sensor [157]. Below we discuss several types of vdW HSs-based devices and their potential applications.

4.1 Transistors

2D materials and vdW HSs hold unique promises for atomically thin transistors, which can exhibit low subthreshold swing, high drive current, and other desirable device properties [160, 161]. In Table 3 [27, 162–175], we summarize some of the recent progress on 2D FETs. Below we discuss 2D-HS-based FETs by dividing them into two categories, lateral and vertical ones, based on the geometry of and direction of current flow in the HSs.

4.1.1 *FETs based on lateral HSs*

It has been theoretically shown that a lateral graphene/h-BCN FET [162] can have I_{on}/I_{off} ratio larger than 10^4, with a gate length of 7 nm and a supply voltage of 0.6 V. Later, a lateral p-type graphene/WSe_2 FET is experimentally demonstrated, with p-doping graphene used to reduce the graphene/WSe_2 junction resistance; this causes the on-current to be significantly increased, and the I_{on}/I_{off} ratio reaches $\sim 10^8$ (Figure 11(a)) [163]. More recently, a lateral MoS_2/NbS_2 FET is predicted to have high on-off ratios (10^6–10^7) and minimal leakage current (on the order of 10^{-8} μA) [164]. It is also predicted that in lateral NbS_2/MoS_2/NbS_2 FETs, the electron transport along the armchair edge shows ballistic transport properties, while along the zigzag edge, it exhibits resonance tunneling transport properties [165].
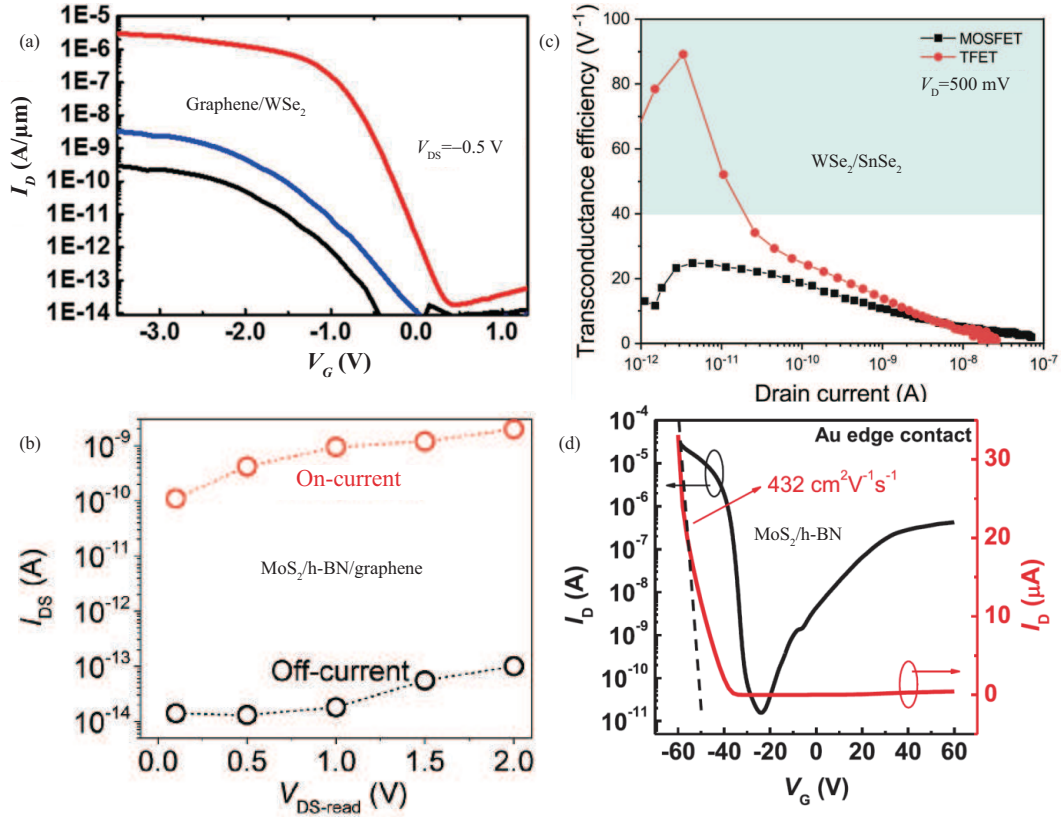
Figure 11 (Color online) (a) Transfer curves of 1L-graphene/WSe$_2$ (red) and multilayer-graphene/WSe$_2$ (blue and black) transistors [163] © 2017 American Chemical Society. (b) Dependence of the on- and off-current on $V_{\text{DS-read}}$ for an MoS$_2$/h-BN/graphene FET, as it is programmed using a voltage pulse (-10 V, 1 s) and erased using a light pulse (50 nW, 1 s) [170] © 2019 John Wiley & Sons. (c) Direct comparison of the transconductance efficiencies of a WSe$_2$/SnSe$_2$ HS and a WSe$_2$ MOSFET. The WSe$_2$/SnSe$_2$ FET reaches peak transconductance efficiency close to 90 V^{-1} and outperforms the MOSFET over the entire subthreshold region [171] © 2020 Springer Nature. (d) Transfer curves of an Au/MoS$_2$/h-BN FET with 1D edge contact in log scale (black) and linear scale (red), measured at room temperature and $V_D = 1$ V [175] © 2019 John Wiley & Sons.

4.1.2 *FETs based on vertical HSs*

FETs based on vertical HSs are much more studied, due to their easier fabrication process compared with that of lateral FETs. For example, h-BN/graphene transistors on flexible substrates have been demonstrated, exhibiting excellent electrical and mechanical properties as well as robust stability [176, 177]. In addition, TMDC/graphene and TMDC/h-BN/graphene FETs have been studied extensively [166–170]. Figure 11(b) shows data from an MoS$_2$/h-BN/graphene HS FET with an extremely low off-current of $\sim 10^{-14}$ A, and a high optical switching on/off current ratio of over $\sim 10^6$ [170].

Besides TMDC/graphene-based FETs, TMDC/TMDC FETs have also been widely studied, with an example shown in Figure 11(c). Compared with WSe$_2$ MOSFET, the WSe$_2$/SnSe$_2$ tunnel FET exhibits a greater on/off current ratio (in excess of 10^5 at $V_{\text{DS}} = 500$ mV) and a larger subthreshold region [171]. Similarly, FETs-based vertical 2D HSs formed by WSe$_2$/SnS$_2$, MoS$_2$/NbS$_2$, and WSe$_2$/MoSe$_2$ HSs all exhibit excellent device performance [27, 172], including, but are not limited to, ultra-low off-state leakage current, high on-off ratio, excellent gate modulation behavior, and high rectification ratio.

While FETs-based vertical 2D HSs have already demonstrated great potential, there is continued effort to further improve their device performance [160, 161, 173, 174, 178]. By choosing the optimal electrode materials [175], a high hole mobility of 432 cm^{2}V^{-1}s^{-1} (Au) and a high $I_{\text{on}}/I_{\text{off}}$ ratio exceeding 10^8 (Pd) are realized in MoS$_2$/h-BN FETs (Figure 11(d)). Other efforts to improve device performance include fabricating highly doped and air-stable devices [160], optimizing the Schottky contacts [161], and applying thermal annealing treatment [178].

Table 3 Performance of various vdW FET devices

HSs	I_{on}/I_{off}	Mobilities (cm^2/Vs)	Gate structures	Ref.
Lateral graphene/WSe$_2$	$\sim 10^8$	84	Top-gate	[163]
Vertical graphene/MoS$_2$	$\sim 10^5$	3000–5000	Back-gate	[168]
Vertical graphene/MoS$_2$	5×10^4	–	Back-gate	[169]
Vertical MoS$_2$/graphene	10^2	600	Conductive-AFM	[167]
Vertical MoTe$_2$/graphene	$\sim 10^5$	–	Top-gate	[174]
Vertical MoS$_2$/h-BN/graphene	10^4–10^6	45	Back-gate	[166]
Vertical MoS$_2$/h-BN/graphene	$\sim 10^6$	–	Two-terminal floating-gate	[170]
Vertical h-BN/MoS$_2$	$> 10^8$	432	Back-gate	[175]
Vertical h-BN/MoS$_2$/h-BN	10^7	49.7	Double-gate	[173]
Vertical WSe$_2$/SnS$_2$	10^7	10.1	Back-gate	[27]
Vertical WSe$_2$/SnSe$_2$	$> 10^5$	1.8	Back-gate	[171]
Vertical MoSe$_2$/WSe$_2$	$\sim 3\times10^5$–6×10^5	2.2 (hole), 15.1 (electron)	Back-gate	[172]

4.2 Photoelectronic devices

Photoelectric devices, such as photodetectors and photovoltaic devices, have been realized in 2D HSs. Unlike conventional 3D p-n junction, 2D vdW HSs do not have any depletion region in the vertical direction, so the interlayer coupling and interfacial effect may affect the interlayer charge transfer and photocarrier generation [179, 180]. This makes 2D vdW HSs-based photoelectric devices interesting for both studying physical mechanisms and exploring novel applications.

4.2.1 *Photoconductive devices (photodetectors)*

Detectivity and detection range are important parameters for photodetectors, so many efforts have been spent on improving these parameters in 2D-based photodetectors. For example, a unipolar barrier photodetector fabricated by WS$_2$/h-BN/PdSe$_2$ vdW HS has been demonstrated [181]. This detector can be used for visible and mid-wavelength infrared light detection, and exhibits an ultralow dark-current density and an ultrahigh light I_{on}/I_{off} ratio, compared with other 2D-based photodetectors at room temperature. In another work, a photodetector based on MoS$_2$/graphene/WSe$_2$ HS has been successfully demonstrated, showing broadband photodetection in the visible to the short-wavelength infrared range at room temperature, as shown in Figure 12(a) [182]. This device exhibits competitive performance, including a specific detectivity of up to 10^{11} Jones in the near-infrared region. In another example, a self-powered photodetector has been achieved using lateral MoS$_2$/WS$_2$ HSs, which exhibits a spectral responsivity of 4.36 mA/W and detectivity of 4.36×10^{13} Jones [183].

4.2.2 *Photovoltaic devices (solar cells)*

2D TMDC HSs are also frequently used for building photovoltaic devices, due to their strong optical absorption, which can be as high as 95% [184]. In particular, 2D TMDC HS systems with type-II band alignments have great potential for such devices. The performance of photovoltaic devices is characterized by many key parameters, such as quantum efficiency, response time, and spectral range. Recently, photovoltaic devices based on vdW HSs with high performance have been widely studied, as well as various improvement methods for device performance. Here we briefly introduce some of the recent progress.

In one example, an h-BN/graphene/TMDC/graphene HS is demonstrated, based on which a high-performance 2D photovoltaic device is realized with large photon absorption and photocurrent production, as well as an extrinsic quantum efficiency of 30% [184]. Further, a number of photovoltaic devices based on WSe$_2$/SnS$_2$ HSs [27], bP/MoTe$_2$ HSs [185], and MoS$_2$/graphene HSs [186] have been successfully designed, mostly with high quantum efficiency, broadband absorption spectral range, and fast photoresponse (Figure 12(b)).

To improve device performance, one demonstrated pathway is electrically tuning the vdW HSs-based devices [186–189]. For example, in a type-II graphene/MoS$_2$/WS$_2$/graphene HS [189], applying back-gate voltage can effectively modulate the photovoltaic effect through tuning the interlayer electron-hole recombination rate, and the photocurrent direction could be reversed by switching the stacking sequences
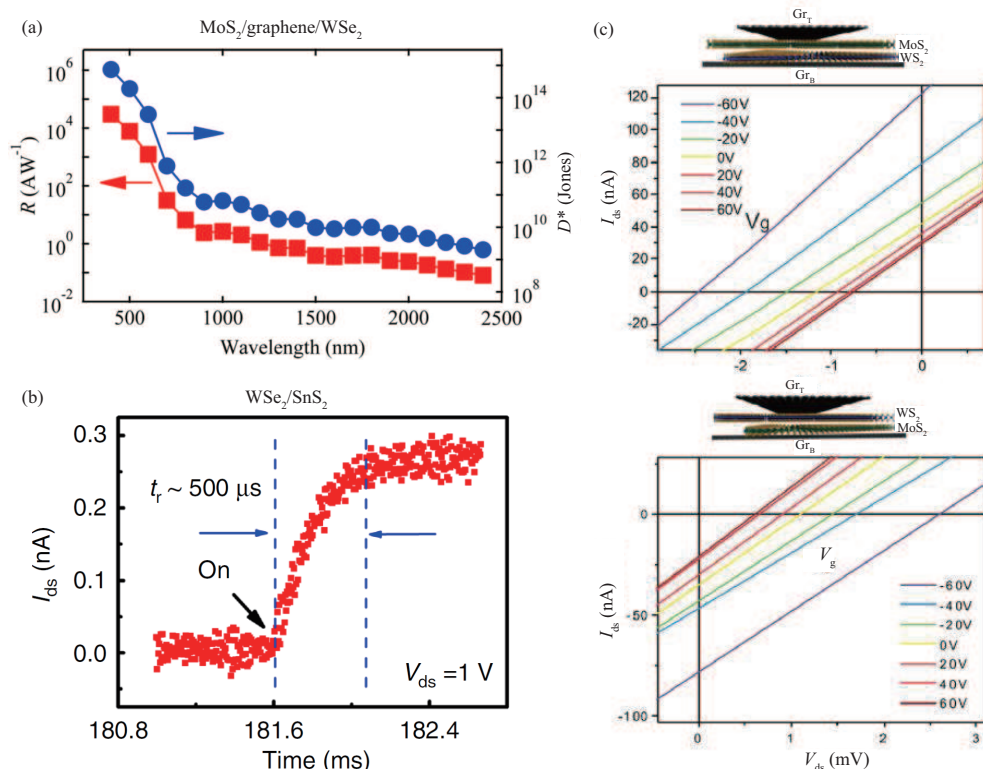
Figure 12 (Color online) (a) Photoresponsivity R (left) and specific detectivity D^* (right) of an MoS_2/graphene/WSe_2 HS device for wavelengths ranging from 400 to 2400 nm. The device was tested in ambient air at $V_{ds} = 1$ V and $V_g = 0$ V [182] © 2016 American Chemical Society. (b) Time-resolved photoresponse of a WSe_2/SnS_2 device with a fast response time of 500 μs measured at $V_{ds} = 1$ V [27] © 2017 Springer Nature. (c) Graphene/WS_2/MoS_2/graphene and graphene/MoS_2/WS_2/graphene vertical devices with various back-gate voltages under the excitation power at 270 μW for 532 nm [189] © 2019 American Chemical Society.

of WS_2 and MoS_2 (Figure 12(c)). This interesting phenomenon is also observed in a graphene/WS_2/h-BN/graphene HS [190].

Beyond existing 2D photovoltaic devices, simulations have predicted numerous photovoltaic devices, offering guidance for future research [191–193]. Type-II $MoSe_2$/SnS_2 HSs with direct-bandgap are predicted as potential candidates for solar cell applications [193], followed by 91 simulated 2D HSs with potentially high power conversion efficiency and thus promising for ultrathin excitonic solar cells [192].

4.3 Sensors

2D materials and their vdW HSs also show vast potential for sensing devices, especially flexible sensors, thanks to their atomically thin structure, large surface-to-volume ratio, and unique electrical, mechanical, and optical properties. Below we briefly survey biosensors, pressure sensors, and gas sensors based on 2D HSs.

4.3.1 *Biosensors*

One broadly-studied sensing application for 2D HSs is biosensing. A common sensing mechanism in 2D HS biosensors is surface plasmon resonance (SPR). A number of SPR-based biosensors have been proposed, including bP/TMDC HSs and bP/graphene HSs [194, 195], graphene/MoS_2 HSs [196] and $PtSe_2$/WS_2 HSs [197]. Such SPR-based vdW HSs biosensors often show high sensitivity, wide linear range, and good detection limit, and have been used to detect protein, DNA, micromolecule, cell, virus, etc. For example, the graphene/MoS_2-based molecule detector exhibits ultrahigh sensitivity, which is about 2000-fold higher than that of conventional SPR sensors [196].

Other sensing mechanisms beyond SPR have also been explored in 2D HSs to demonstrate functions and devices like DNA detection [198–200] and visual sensor [201]. Figure 13(a) schematically illustrates the charge distribution of DNA on graphene/MoS_2 HS, and Figure 13(b) shows the representative PL spectra,

which are used for label-free and selective detection of DNA hybridization [198]. In this device, the graphene serves as a protection layer to prevent the reaction between MoS_2 and the ambient environment, as well as a biocompatible interface layer to host DNA molecules on its surfaces. The PL intensity of the MoS_2 layer increases with the concentration of the added target DNA, which can be performed at ultralow concentration. In another example, a high-density and hemispherically-curved image sensor array is designed, leveraging the atomically thin MoS_2/graphene HS and strain-releasing device designs [201].

4.3.2 *Pressure sensors*

Based on the sensitivity of 2D vdW structures to pressure, one can use them to construct atomically thin pressure sensors. In one example, the performance of a graphene/h-BN/graphene HS used for pressure sensing is calculated [202]. The results indicate that a sensor with 6 h-BN layers shows optimal performance, which is highly sensitive to pressure while insensitive to temperature. As the number of h-BN layers increases, the responsivity of the pressure sensor increases, with the trade-offs such as increased non-linearity and reduced tunneling current.

Figure 13(c) shows the time-dependent response of another 2D pressure sensor based on bP/graphene HS. The hybridized sensor exhibits a high thermal index, good strain sensitivity, and excellent durability (over 18400 cycles), promising for wearable (even on-skin) temperature-strain sensing applications [203]. In addition to pressure sensing, such bP/graphene hybrid HS can also be used for humidity sensing [204], which shows improved stability than bP-based humidity sensors.

4.3.3 *Gas sensors*

2D vdW HSs have also been widely used for gas sensing, such as graphene/MoS_2 HSs as NO_2 sensors [205–207] and toluene sensors [208]. These sensors often have high responsivity, good selectivity, low detection limit, large detection range, and broad working temperature range. Figure 13(d) shows the response of a mechanically stable (upon bending 5000 times) NO_2 sensor based on graphene/MoS_2 HSs [205], in which the patterned graphene is used for charge collection, and the response of MoS_2 can detect an NO_2 concentration as low as 1.2 ppm.

TMDC/TMDC HS-based gas sensors, such as those based on MoS_2/WS_2, WSe_2/WS_2, and MoS_2/WSe_2 HSs, have also been studied. In one study, the response of an MoS_2/WS_2 gas sensor towards different gases is studied, showing improved selectivity for NO_2 compared to MoS_2 sensors [209]. It is also theoretically predicted that p-type WSe_2/WS_2 and n-type MoS_2/WSe_2 HSs can be used as photovoltaic self-powered gas sensors [210], capable of detecting NO_2 and NH_3 gases with high responsivity and selectivity without external bias voltage (Figure 13(e)).

4.4 Memory devices

2D vdW HSs also hold promises for building future memory devices. A survey of current memory technologies [211] outlines a roadmap for non-volatile memory to gradually replace conventional flash memory, suggesting that the outstanding electrical and magnetic properties of 2D vdW HSs are promising for addressing some of the key challenges in this field, such as low material reliability and high off-state current [158]. Recent studies on vdW HSs-based non-volatile memories have suggested that these memory devices can have excellent erase/program ratio, enduring performance [212], and ultrahigh writing speed [211].

For example, a conceptual non-volatile optoelectronic memory based on MoS_2/bP/MoS_2 HSs has been demonstrated [213]. Figure 14(a) shows the readout current of this device as a function of the number of applied laser pulses, which gives the evidence that the device can be operated under eleven storage states. Non-volatile memory devices based on MoS_2/graphene HS have also been studied [214], in which the current in the MoS_2 layer is highly sensitive to the presence of charges in the charge trapping layer, resulting in a factor of 10^4 difference between the memory program and erase states.

Recent studies show that inserting a barrier layer (e.g., h-BN) into 2D HSs can improve the performance of a memory device [215]. In this case, a tunneling random access memory is fabricated by inserting an h-BN layer into an MoS_2/graphene HS to form an MoS_2/h-BN/graphene structure. Figure 14(b) compares the off current and on/off ratio of three types of RAM (TRAM, PRAM, and RRAM; standing for tunneling, phase change, and resistive random access memory) [158]. With effective charge tunneling
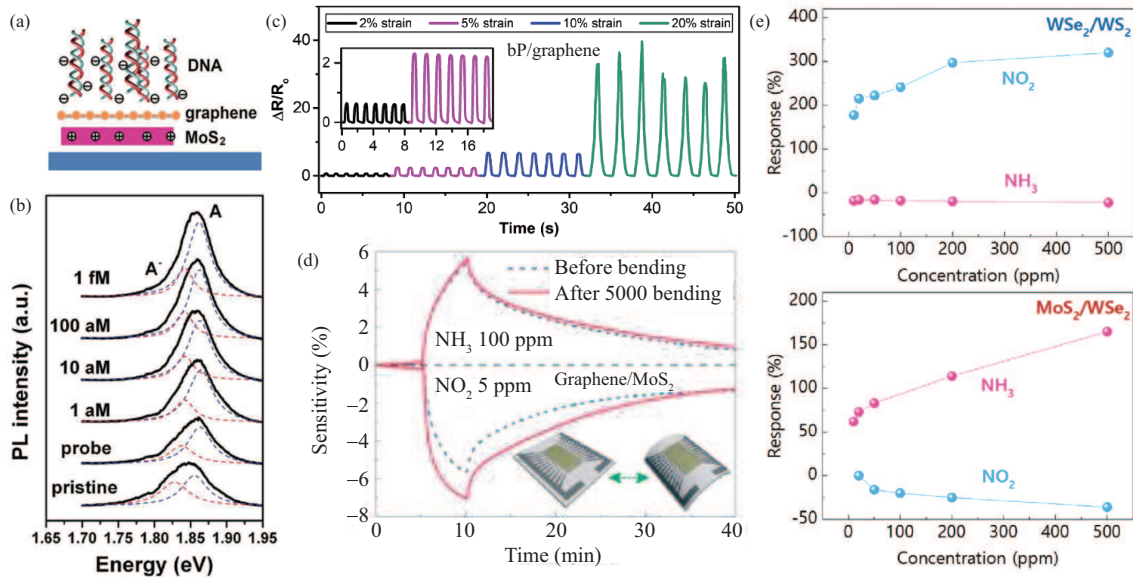
Figure 13 (Color online) (a) Schematic illustration of charge distribution of DNA on a graphene/MoS$_2$ HS [198] © 2014 John Wiley & Sons. (b) PL peak of the A-trion (red dashed line) and A exciton (blue dashed line) responding differently to target DNA concentration in a graphene/MoS$_2$ HS [198] © 2014 John Wiley & Sons. (c) Time-dependent resistance response to strains from 2% to 20% of a bP/graphene sensor [203] © 2021 Wiley-VCH GmbH. (d) Response to different gases of a flexible graphene/MoS$_2$ device before and after bending. Inset: schematic of the bending [205] © 2015 American Chemical Society. (e) Calculated response of WSe$_2$/WS$_2$ and MoS$_2$/WSe$_2$ gas sensor corresponding to each gas concentration of NO$_2$ and NH$_3$ [210] © 2020 Wiley-VCH GmbH.
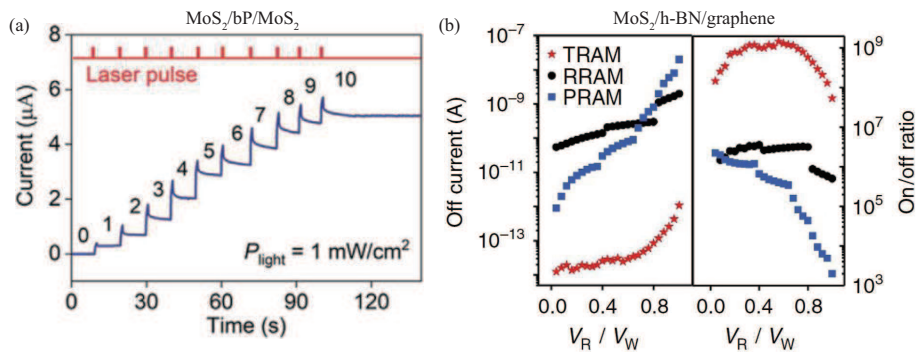

Figure 14 (Color online) (a) Readout current as the number of applied laser pulses increases in an MoS$_2$/bP/MoS$_2$ HS [213] © 2021 Wiley-VCH GmbH. (b) Off current (left panel) and on/off ratio (right panel) of three types of RAM devices with MoS$_2$/h-BN/graphene structure [158] © 2016 Springer Nature.

through the h-BN layer and stored charges in the graphene layer, the TRAM device shows a low off-state current of 10^{-14} A, and thus an ultrahigh on/off ratio over 10^9.

4.5   Mechanical resonators

2D vdW HSs have also been demonstrated in building atomically thin mechanical resonators, with resonance frequencies typically in the high- and very-high-frequency (HF and VHF) bands. Furthermore, the material choice and stacking degree of freedom offer researchers new tools, for tailoring elastic modulus and thus the resonant response of the 2D structure, and for studying interlayer interactions such as friction and sliding.

For example, resonators based on MoS$_2$/graphene and h-BN/graphene heterostructures have been successfully demonstrated [216, 217], showing robust nanomechanical resonances and gate tunability in both frequency and quality factors. Figure 15(a) shows the frequency tuning curve in a graphene/MoS$_2$ HS resonator, where a kink is clearly visible. This is explained as the onset of an interlayer slippage in the heterostructure.

Interestingly, density functional theory simulation suggests the presence of a local pinning effect at
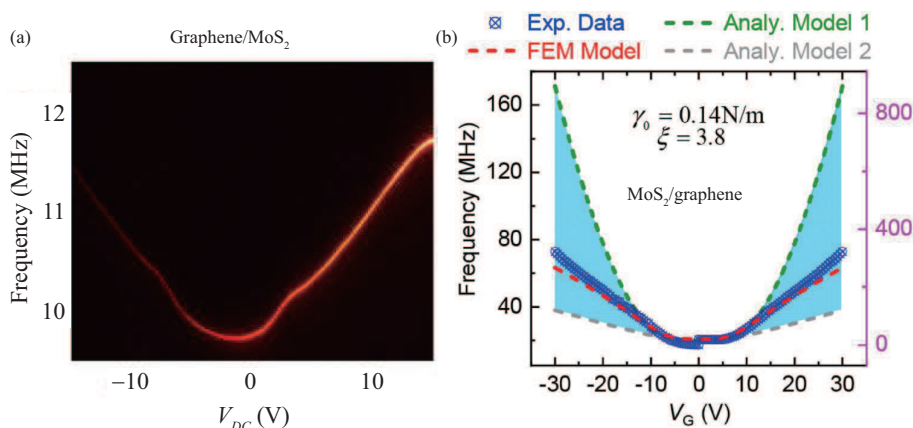
Figure 15 (Color online) (a) Fundamental mode frequency tuning by sweeping gate voltage of graphene/MoS$_2$ resonator [218] © 2018 American Chemical Society. (b) Measured frequency tuning Vs gate voltage of MoS$_2$/graphene resonator [219] © 2021 American Chemical Society.

ripples and folds in the HS, which determines the onset of such an interlayer process [218]. In contrast, in another work [219], such kink has not been observed in resonators made from monolayer MoS$_2$ stacked on single-, tri-, and few-layer graphene by a clean, all-dry transfer method. The devices exhibit an ultrawide frequency tuning range (Figure 15(b)), suggesting a clean interface and thus strong vdW bonding between the layers.

5 Conclusion and outlook

We have above surveyed recent progress in studying 2D vdW HSs, including fabrication methods, material properties, and device applications. While this family of 2D structures exhibits many exceptional properties and intriguing device performance, further studies on 2D vdW HSs still face important challenges, and several scientific questions remain unexplored. This offers new opportunities for 2D HS study that can potentially lead to important breakthroughs. Here we discuss a few such examples.

(1) Further development of growth techniques. Effective methods to synthesize large-area, high-quality, low-cost 2D HSs are becoming increasingly important for enabling future device applications. In addition, the growth of 2D HSs consisting of air-sensitive materials (such as CrI$_3$) remains yet to be demonstrated, hindering further development of 2D magnetic HSs. Solving the growth challenge will therefore greatly enable further exploration and future application of 2D HSs.

(2) Investigation of twistronics in 2D HSs beyond BLG. Twistronics is an emerging field in condensed matter physics, and has been actively studied over the last couple of years. TBG with magic angle is an extensively studied system for the exploration of twistronics. More recently, twisted tri-layer graphene and Moiré superlattices based on bilayer TMDC HSs have also started to attract increasing research interest. Meanwhile, other twisted 2D HSs systems, such as twisted bilayer based on 2D magnets, have rarely been studied. Modulation of twisted bilayer by external fields, such as electric and magnetic fields, is also open for further exploration. Such a study will likely lead to new findings and novel physical processes.

(3) Exploration of 2D magnetic memory devices. 2D magnetic HSs (e.g., TMDC/CrX$_3$, CrX$_3$/CrX$_3$ HSs) have great potential to make new types of magneto-optic, magneto-electric, and spintronic devices. However, to date, 2D HSs-based memory devices are mostly based on nonmagnetic 2D HSs. Therefore, there is a clear opportunity of exploring magnetic memory devices based on 2D magnets by leveraging their spin degree of freedom (rather than the charge degree of freedom as in existing 2D HS memories).

References

1 Novoselov K S, Geim A K, Morozov S V, et al. Electric field effect in atomically thin carbon films. Science, 2004, 306: 666–669

2 Koenig S P, Doganov R A, Schmidt H, et al. Electric field effect in ultrathin black phosphorus. Appl Phys Lett, 2014, 104: 103106

3 Wang Q H, Kalantar-Zadeh K, Kis A, et al. Electronics and optoelectronics of two-dimensional transition metal dichalcogenides. Nat Nanotechnol, 2012, 7: 699–712

4 Corso M, Auwärter W, Muntwiler M, et al. Boron nitride nanomesh. Science, 2004, 303: 217–220

5 Huang B, Clark G, Navarro-Moratalla E, et al. Layer-dependent ferromagnetism in a van der Waals crystal down to the monolayer limit. Nature, 2017, 546: 270–273

6 Gong C, Li L, Li Z, et al. Discovery of intrinsic ferromagnetism in two-dimensional van der Waals crystals. Nature, 2017, 546: 265–269

7 Tan C, Lee J, Jung S G, et al. Hard magnetic properties in nanoflake van der Waals Fe_3GeTe_2. Nat Commun, 2018, 9: 1554

8 Otrokov M M, Klimovskikh I I, Bentmann H, et al. Prediction and observation of an antiferromagnetic topological insulator. Nature, 2019, 576: 416–422

9 Zatko V, Dubois S M M, Godel F, et al. Band-gap landscape engineering in large-scale 2D semiconductor van der Waals heterostructures. ACS Nano, 2021, 15: 7279–7289

10 Yang W, Kawai H, Bosman M, et al. Interlayer interactions in 2D WS_2/MoS_2 heterostructures monolithically grown by in situ physical vapor deposition. Nanoscale, 2018, 10: 22927–22936

11 Heilmann M, Bashouti M, Riechert H, et al. Defect mediated van der Waals epitaxy of hexagonal boron nitride on graphene. 2D Mater, 2018, 5: 025004

12 Ci L, Song L, Jin C, et al. Atomic layers of hybridized boron nitride and graphene domains. Nat Mater, 2010, 9: 430–435

13 Liu Z, Song L, Zhao S, et al. Direct growth of graphene/hexagonal boron nitride stacked layers. Nano Lett, 2011, 11: 2032–2037

14 Chang C K, Kataria S, Kuo C C, et al. Band gap engineering of chemical vapor deposited graphene by *in situ* BN doping. ACS Nano, 2013, 7: 1333–1341

15 Sutter P, Cortes R, Lahiri J, et al. Interface formation in monolayer graphene-boron nitride heterostructures. Nano Lett, 2012, 12: 4869–4874

16 Liu Z, Ma L, Shi G, et al. In-plane heterostructures of graphene and hexagonal boron nitride with controlled domain sizes. Nat Nanotechnol, 2013, 8: 119–124

17 Liu L, Park J, Siegel D A, et al. Heteroepitaxial growth of two-dimensional hexagonal boron nitride templated by graphene edges. Science, 2014, 343: 163–167

18 Gong Y, Shi G, Zhang Z, et al. Direct chemical conversion of graphene to boron- and nitrogen- and carbon-containing atomic layers. Nat Commun, 2014, 5: 3193

19 Gao T, Song X, Du H, et al. Temperature-triggered chemical switching growth of in-plane and vertically stacked graphene-boron nitride heterostructures. Nat Commun, 2015, 6: 6835

20 Tang S, Wang H, Wang H S, et al. Silane-catalysed fast growth of large single-crystalline graphene on hexagonal boron nitride. Nat Commun, 2015, 6: 6499

21 Li Q, Zhao Z, Yan B, et al. Nickelocene-precursor-facilitated fast growth of graphene/h-BN vertical heterostructures and its applications in OLEDs. Adv Mater, 2017, 29: 1701325

22 Zhang C, Zhao S, Jin C, et al. Direct growth of large-area graphene and boron nitride heterostructures by a co-segregation method. Nat Commun, 2015, 6: 6519

23 Duan X, Wang C, Shaw J C, et al. Lateral epitaxial growth of two-dimensional layered semiconductor heterojunctions. Nat Nanotechnol, 2014, 9: 1024–1030

24 Huang C, Wu S, Sanchez A M, et al. Lateral heterojunctions within monolayer $MoSe_2$-WSe_2 semiconductors. Nat Mater, 2014, 13: 1096–1101

25 Gong Y, Lei S, Ye G, et al. Two-step growth of two-dimensional $WSe_2/MoSe_2$ heterostructures. Nano Lett, 2015, 15: 6135–6141

26 Xue Y, Zhang Y, Liu Y, et al. Scalable production of a few-layer MoS_2/WS_2 vertical heterojunction array and its application for photodetectors. ACS Nano, 2016, 10: 573–580

27 Yang T, Zheng B, Wang Z, et al. van der Waals epitaxial growth and optoelectronics of large-scale WSe_2/SnS_2 vertical bilayer p-n junctions. Nat Commun, 2017, 8: 1906

28 Lee J, Pak S, Lee Y W, et al. Direct epitaxial synthesis of selective two-dimensional lateral heterostructures. ACS Nano, 2019, 13: 13047–13055

29 Wu X, Li H, Liu H, et al. Spatially composition-modulated two-dimensional $WS_{2x}Se_{2(1-x)}$ nanosheets. Nanoscale, 2017, 9: 4707–4712

30 Zheng B, Ma C, Li D, et al. Band alignment engineering in two-dimensional lateral heterostructures. J Am Chem Soc, 2018, 140: 11193–11197

31 Gong Y, Lin J, Wang X, et al. Vertical and in-plane heterostructures from WS_2/MoS_2 monolayers. Nat Mater, 2014, 13: 1135–1142

32 Shi J, Tong R, Zhou X, et al. Temperature-mediated selective growth of MoS_2/WS_2 and WS_2/MoS_2 vertical stacks on Au foils for direct photocatalytic applications. Adv Mater, 2016, 28: 10664–10672

33 Yoo Y, Degregorio Z P, Johns J E. Seed crystal homogeneity controls lateral and vertical heteroepitaxy of monolayer MoS_2 and WS_2. J Am Chem Soc, 2015, 137: 14281–14287

34 Sahoo P K, Memaran S, Xin Y, et al. One-pot growth of two-dimensional lateral heterostructures via sequential edge-epitaxy. Nature, 2018, 553: 63–67

35 Zhang Z, Chen P, Duan X, et al. Robust epitaxial growth of two-dimensional heterostructures, multiheterostructures, and superlattices. Science, 2017, 357: 788–792

36 Kobayashi Y, Yoshida S, Maruyama M, et al. Continuous heteroepitaxy of two-dimensional heterostructures based on layered chalcogenides. ACS Nano, 2019, 13: 7527–7535

37　Xie S, Tu L, Han Y, et al. Coherent, atomically thin transition-metal dichalcogenide superlattices with engineered strain. Science, 2018, 359: 1131–1136

38　Zhao B, Wan Z, Liu Y, et al. High-order superlattices by rolling up van der Waals heterostructures. Nature, 2021, 591: 385–390

39　Jin G, Lee C S, Okello O F N, et al. Heteroepitaxial van der Waals semiconductor superlattices. Nat Nanotechnol, 2021, 16: 1092–1098

40　Luican A, Li G, Reina A, et al. Single-layer behavior and its breakdown in twisted graphene layers. Phys Rev Lett, 2011, 106: 126802

41　Lu C C, Lin Y C, Liu Z, et al. Twisting bilayer graphene superlattices. ACS Nano, 2013, 7: 2587–2594

42　Liu K, Zhang L, Cao T, et al. Evolution of interlayer coupling in twisted molybdenum disulfide bilayers. Nat Commun, 2014, 5: 4966

43　Zheng S, Sun L, Zhou X, et al. Coupling and interlayer exciton in twist-stacked WS_2 bilayers. Adv Opt Mater, 2015, 3: 1600–1605

44　Sun L, Wang Z, Wang Y, et al. Hetero-site nucleation for growing twisted bilayer graphene with a wide range of twist angles. Nat Commun, 2021, 12: 2391

45　Reina A, Son H, Jiao L, et al. Transferring and identification of single- and few-layer graphene on arbitrary substrates. J Phys Chem C, 2008, 112: 17741–17744

46　Dean C R, Young A F, Meric I, et al. Boron nitride substrates for high-quality graphene electronics. Nat Nanotechnol, 2010, 5: 722–726

47　Leon J A, Mamani N C, Rahim A, et al. Transferring few-layer graphene sheets on hexagonal boron nitride substrates for fabrication of graphene devices. Graphene, 2014, 03: 25–35

48　Zomer P J, Dash S P, Tombros N, et al. A transfer technique for high mobility graphene devices on commercially available hexagonal boron nitride. Appl Phys Lett, 2011, 99: 232104

49　Zomer P J, Guimarães M H D, Brant J C, et al. Fast pick up technique for high quality heterostructures of bilayer graphene and hexagonal boron nitride. Appl Phys Lett, 2014, 105: 013101

50　Wang J I J, Yang Y, Chen Y A, et al. Electronic transport of encapsulated graphene and WSe_2 devices fabricated by pick-up of prepatterned hBN. Nano Lett, 2015, 15: 1898–1903

51　Huang Z, Alharbi A, Mayer W, et al. Versatile construction of van der Waals heterostructures using a dual-function polymeric film. Nat Commun, 2020, 11: 3029

52　Pizzocchero F, Gammelgaard L, Jessen B S, et al. The hot pick-up technique for batch assembly of van der Waals heterostructures. Nat Commun, 2016, 7: 11894

53　Purdie D G, Pugno N M, Taniguchi T, et al. Cleaning interfaces in layered materials heterostructures. Nat Commun, 2018, 9: 5387

54　Castellanos-Gomez A, Buscema M, Molenaar R, et al. Deterministic transfer of two-dimensional materials by all-dry viscoelastic stamping. 2D Mater, 2014, 1: 011002

55　Yang R, Zheng X, Wang Z, et al. Multilayer MoS_2 transistors enabled by a facile dry-transfer technique and thermal annealing. J Vacuum Sci Tech B, 2014, 32: 061203

56　Cao Y, Fatemi V, Fang S, et al. Unconventional superconductivity in magic-angle graphene superlattices. Nature, 2018, 556: 43–50

57　Cao Y, Fatemi V, Demir A, et al. Correlated insulator behaviour at half-filling in magic-angle graphene superlattices. Nature, 2018, 556: 80–84

58　Xu Y, Liu S, Rhodes D A, et al. Correlated insulating states at fractional fillings of Moiré superlattices. Nature, 2020, 587: 214–218

59　Liu E, Barré E, van Baren J, et al. Signatures of Moiré trions in $WSe_2/MoSe_2$ heterobilayers. Nature, 2021, 594: 46–50

60　Chen X D, Xin W, Jiang W S, et al. High-precision twist-controlled bilayer and trilayer graphene. Adv Mater, 2016, 28: 2563–2570

61　Carozo V, Almeida C M, Ferreira E H M, et al. Raman signature of graphene superlattices. Nano Lett, 2011, 11: 4527–4534

62　Kim K, Yankowitz M, Fallahazad B, et al. van der Waals heterostructures with high accuracy rotational alignment. Nano Lett, 2016, 16: 1989–1995

63　Wang K, Huang B, Tian M, et al. Interlayer coupling in twisted WSe_2/WS_2 bilayer heterostructures revealed by optical spectroscopy. ACS Nano, 2016, 10: 6612–6622

64　Xia J, Yan J, Wang Z, et al. Strong coupling and pressure engineering in WSe_2-$MoSe_2$ heterobilayers. Nat Phys, 2021, 17: 92–98

65　Fu X, Li F, Lin J F, et al. Coupling-assisted renormalization of excitons and vibrations in compressed $MoSe_2$-WSe_2 heterostructure. J Phys Chem C, 2018, 122: 5820–5828

66　Lee Y Y, Hu Z, Wang X, et al. Progressive micromodulation of interlayer coupling in stacked WS_2/WSe_2 heterobilayers tailored by a focused laser beam. ACS Appl Mater Interf, 2018, 10: 37396–37406

67　Baranowski M, Surrente A, Klopotowski L, et al. Probing the interlayer exciton physics in a $MoS_2/MoSe_2/MoS_2$ van der Waals heterostructure. Nano Lett, 2017, 17: 6360–6365

68　Rivera P, Schaibley J R, Jones A M, et al. Observation of long-lived interlayer excitons in monolayer $MoSe_2$-WSe_2 heterostructures. Nat Commun, 2015, 6: 6242

69　Li Z, Lu X, Leon D F C, et al. Interlayer exciton transport in $MoSe_2/WSe_2$ heterostructures. ACS Nano, 2021, 15: 1539–1547

70　Li Y, Xu C Y, Qin J K, et al. Tuning the excitonic states in MoS_2/graphene van der Waals heterostructures via electrochemical gating. Adv Funct Mater, 2016, 26: 293–302

71　Unuchek D, Ciarrocchi A, Avsar A, et al. Room-temperature electrical control of exciton flux in a van der Waals heterostructure. Nature, 2018, 560: 340–344

72　Mouri S, Zhang W, Kozawa D, et al. Thermal dissociation of inter-layer excitons in $MoS_2/MoSe_2$ hetero-bilayers. Nanoscale,

2017, 9: 6674–6679

73 Meng Y, Wang T, Jin C, et al. Electrical switching between exciton dissociation to exciton funneling in MoSe$_2$/WS$_2$ heterostructure. Nat Commun, 2020, 11: 2640

74 Miller B, Steinhoff A, Pano B, et al. Long-lived direct and indirect interlayer excitons in van der Waals heterostructures. Nano Lett, 2017, 17: 5229–5237

75 Kremser M, Brotons-Gisbert M, Knörzer J, et al. Discrete interactions between a few interlayer excitons trapped at a MoSe$_2$-WSe$_2$ heterointerface. npj 2D Mater Appl, 2020, 4: 8

76 Hsu W T, Lin B H, Lu L S, et al. Tailoring excitonic states of van der Waals bilayers through stacking configuration, band alignment, and valley spin. Sci Adv, 2019, 5: eaax7407

77 Merkl P, Mooshammer F, Steinleitner P, et al. Ultrafast transition between exciton phases in van der Waals heterostructures. Nat Mater, 2019, 18: 691–696

78 Kravtsov V, Liubomirov A D, Cherbunin R V, et al. Spin-valley dynamics in alloy-based transition metal dichalcogenide heterobilayers. 2D Mater, 2021, 8: 025011

79 Nagler P, Ballottin M V, Mitioglu A A, et al. Giant magnetic splitting inducing near-unity valley polarization in van der Waals heterostructures. Nat Commun, 2017, 8: 1551

80 Cho C, Wong J, Taqieddin A, et al. Highly strain-tunable interlayer excitons in MoS$_2$/WSe$_2$ heterobilayers. Nano Lett, 2021, 21: 3956–3964

81 Wang F, Wang J, Guo S, et al. Tuning coupling behavior of stacked heterostructures based on MoS$_2$, WS$_2$ and WSe$_2$. Sci Rep, 2017, 7: 44712

82 Fang H, Battaglia C, Carraro C, et al. Strong interlayer coupling in van der Waals heterostructures built from single-layer chalcogenides. Proc Natl Acad Sci USA, 2014, 111: 6198–6202

83 Jin C, Regan E C, Yan A, et al. Observation of Moiré excitons in WSe$_2$/WS$_2$ heterostructure superlattices. Nature, 2019, 567: 76–80

84 Zhang L, Wu F, Hou S, et al. van der Waals heterostructure polaritons with Moiré-induced nonlinearity. Nature, 2021, 591: 61–65

85 Hong X, Kim J, Shi S F, et al. Ultrafast charge transfer in atomically thin MoS$_2$/WS$_2$ heterostructures. Nat Nanotechnol, 2014, 9: 682–686

86 He J, Kumar N, Bellus M Z, et al. Electron transfer and coupling in graphene-tungsten disulfide van der Waals heterostructures. Nat Commun, 2014, 5: 5622

87 Zhang X, He D, Yi L, et al. Electron dynamics in MoS$_2$-graphite heterostructures. Nanoscale, 2017, 9: 14533–14539

88 Peng B, Yu G, Liu X, et al. Ultrafast charge transfer in MoS$_2$/WSe$_2$ p-n heterojunction. 2D Mater, 2016, 3: 025020

89 Chen H, Wen X, Zhang J, et al. Ultrafast formation of interlayer hot excitons in atomically thin MoS$_2$/WS$_2$ heterostructures. Nat Commun, 2016, 7: 12512

90 Quan J, Linhart L, Lin M L, et al. Phonon renormalization in reconstructed MoS$_2$ Moiré superlattices. Nat Mater, 2021, 20: 1100–1105

91 Leng Y C, Lin M L, Zhou Y, et al. Intrinsic effect of interfacial coupling on the high-frequency intralayer modes in twisted multilayer MoTe$_2$. Nanoscale, 2021, 13: 9732–9739

92 Ge M, Su Y, Wang H, et al. Interface depended electronic and magnetic properties of vertical CrI$_3$/WSe$_2$ heterostructures. RSC Adv, 2019, 9: 14766–14771

93 Hidalgo-Sacoto R, Gonzalez R I, Vogel E E, et al. Magnon valley Hall effect in CrI$_3$-based van der Waals heterostructures. Phys Rev B, 2020, 101: 205425

94 Zhang H, Yang W, Ning Y, et al. Abundant valley-polarized states in two-dimensional ferromagnetic van der Waals heterostructures. Phys Rev B, 2020, 101: 205404

95 Rahman S, Liu B, Wang B, et al. Giant photoluminescence enhancement and resonant charge transfer in atomically thin two-dimensional Cr$_2$Ge$_2$Te$_6$/WS$_2$ heterostructures. ACS Appl Mater Interf, 2021, 13: 7423–7433

96 Zollner K, Junior P E F, Fabian J. Proximity exchange effects in MoSe$_2$ and WSe$_2$ heterostructures with CrI$_3$: twist angle, layer, and gate dependence. Phys Rev B, 2019, 100: 085128

97 Zhong D, Seyler K L, Linpeng X, et al. Layer-resolved magnetic proximity effect in van der Waals heterostructures. Nat Nanotechnol, 2020, 15: 187–191

98 Zhang X X, Li L, Weber D, et al. Gate-tunable spin waves in antiferromagnetic atomic bilayers. Nat Mater, 2020, 19: 838–842

99 Zhong D, Seyler K L, Linpeng X, et al. van der Waals engineering of ferromagnetic semiconductor heterostructures for spin and valleytronics. Sci Adv, 2017, 3: e1603113

100 Mukherjee A, Shayan K, Li L, et al. Observation of site-controlled localized charged excitons in CrI$_3$/WSe$_2$ heterostructures. Nat Commun, 2020, 11: 5502

101 Lyons T P, Gillard D, Molina-Sánchez A, et al. Interplay between spin proximity effect and charge-dependent exciton dynamics in MoSe$_2$/CrBr$_3$ van der Waals heterostructures. Nat Commun, 2020, 11: 6021

102 Seyler K L, Zhong D, Huang B, et al. Valley manipulation by optically tuning the magnetic proximity effect in WSe$_2$/CrI$_3$ heterostructures. Nano Lett, 2018, 18: 3823–3828

103 Lin C, Li Y, Wei Q, et al. Enhanced valley splitting of transition-metal dichalcogenide by vacancies in robust ferromagnetic insulating chromium trihalides. ACS Appl Mater Interf, 2019, 11: 18858–18864

104 Sun Y Y, Shang L, Ju W, et al. Tuning valley polarization in two-dimensional ferromagnetic heterostructures. J Mater Chem C, 2019, 7: 14932–14937

105 Subhan F, Hong J. Large valley splitting and enhancement of curie temperature in a two-dimensional VI$_3$/CrI$_3$ heterostructure. J Phys Chem C, 2020, 124: 7156–7162

106 Li L, Jiang S, Wang Z, et al. Electrical switching of valley polarization in monolayer semiconductors. Phys Rev Mater, 2020, 4: 104005

107 Ciorciaro L, Kroner M, Watanabe K, et al. Observation of magnetic proximity effect using resonant optical spectroscopy of an electrically tunable $MoSe_2/CrBr_3$ heterostructure. Phys Rev Lett, 2020, 124: 197401

108 Xie J, Jia L, Shi H, et al. Electric field mediated large valley splitting in the van der Waals heterostructure WSe_2/CrI_3. Jpn J Appl Phys, 2019, 58: 010906

109 Zhang Z, Ni X, Huang H, et al. Valley splitting in the van der Waals heterostructure WSe_2/CrI_3: the role of atom superposition. Phys Rev B, 2019, 99: 115441

110 Hu T, Zhao G, Gao H, et al. Manipulation of valley pseudospin in WSe_2/CrI_3 heterostructures by the magnetic proximity effect. Phys Rev B, 2020, 101: 125401

111 Behera S K, Bora M, Chowdhury S S P, et al. Proximity effects in graphene and ferromagnetic $CrBr_3$ van der Waals heterostructures. Phys Chem Chem Phys, 2019, 21: 25788–25796

112 Tang C, Zhang Z, Lai S, et al. Magnetic proximity effect in graphene/$CrBr_3$ van der Waals heterostructures. Adv Mater, 2020, 32: 1908498

113 Wu Y, Cui Q, Zhu M, et al. Magnetic exchange field modulation of quantum hall ferromagnetism in 2D van der Waals $CrCl_3$/graphene heterostructures. ACS Appl Mater Interf, 2021, 13: 10656–10663

114 Zhang J, Zhao B, Zhou T, et al. Strong magnetization and Chern insulators in compressed graphene/CrI_3 van der Waals heterostructures. Phys Rev B, 2018, 97: 085401

115 Farooq M U, Hong J. Switchable valley splitting by external electric field effect in graphene/CrI_3 heterostructures. npj 2D Mater Appl, 2019, 3: 3

116 Zhang L, Huang X, Dai H, et al. Proximity-coupling-induced significant enhancement of coercive field and curie temperature in 2D van der Waals heterostructures. Adv Mater, 2020, 32: 2002032

117 Tan X, Ding L, Du G F, et al. Spin caloritronics in two-dimensional $CrI_3/NiCl_2$ van der Waals heterostructures. Phys Rev B, 2021, 103: 115415

118 Fu H, Liu C X, Yan B. Exchange bias and quantum anomalous Hall effect in the $MnBi_2Te_4/CrI_3$ heterostructure. Sci Adv, 2020, 6: eaaz0948

119 Zhu R, Zhang W, Shen W, et al. Exchange bias in van der Waals $CrCl_3/Fe_3GeTe_2$ heterostructures. Nano Lett, 2020, 20: 5030–5035

120 Manna P K, Yusuf S M. Two interface effects: exchange bias and magnetic proximity. Phys Rep, 2014, 535: 61–99

121 Pan L, Huang L, Zhong M, et al. Large tunneling magnetoresistance in magnetic tunneling junctions based on two-dimensional CrX_3 (X = Br, I) monolayers. Nanoscale, 2018, 10: 22196–22202

122 Li X, Lü J T, Zhang J, et al. Spin-dependent transport in van der Waals magnetic tunnel junctions with Fe_3GeTe_2 electrodes. Nano Lett, 2019, 19: 5133–5139

123 Lin Z, Chen X. Ultrathin scattering spin filter and magnetic tunnel junction implemented by ferromagnetic 2D van der Waals material. Adv Electron Mater, 2020, 6: 1900968

124 Pan L, Wen H, Huang L, et al. Two-dimensional XSe_2 (X = Mn, V) based magnetic tunneling junctions with high curie temperature. Chin Phys B, 2019, 28: 107504

125 Yan Z, Zhang R, Dong X, et al. Significant tunneling magnetoresistance and excellent spin filtering effect in CrI_3-based van der Waals magnetic tunnel junctions. Phys Chem Chem Phys, 2020, 22: 14773–14780

126 Lin H, Yan F, Hu C, et al. Spin-valve effect in $Fe_3GeTe_2/MoS_2/Fe_3GeTe_2$ van der Waals heterostructures. ACS Appl Mater Interf, 2020, 12: 43921–43926

127 Soriano D, Lado J L. Exchange-bias controlled correlations in magnetically encapsulated twisted van der Waals dichalcogenides. J Phys D-Appl Phys, 2020, 53: 474001

128 Klein D R, MacNeill D, Lado J L, et al. Probing magnetism in 2D van der Waals crystalline insulators via electron tunneling. Science, 2018, 360: 1218–1222

129 Song T, Cai X, Tu M W Y, et al. Giant tunneling magnetoresistance in spin-filter van der Waals heterostructures. Science, 2018, 360: 1214–1218

130 Wang Z, Gutiérrez-Lezama I, Ubrig N, et al. Very large tunneling magnetoresistance in layered magnetic semiconductor CrI_3. Nat Commun, 2018, 9: 2516

131 Song T, Fei Z, Yankowitz M, et al. Switching 2D magnetic states via pressure tuning of layer stacking. Nat Mater, 2019, 18: 1298–1302

132 Chen X R, Chen W, Shao L B, et al. Engineering chiral edge states in two-dimensional topological insulator/ferromagnetic insulator heterostructures. Phys Rev B, 2019, 99: 085417

133 Heath J J, Costa M, Buongiorno-Nardelli M, et al. Role of quantum confinement and interlayer coupling in CrI_3-graphene magnetic tunnel junctions. Phys Rev B, 2020, 101: 195439

134 Avsar A, Tan J Y, Luo X, et al. van der Waals bonded Co/h-BN contacts to ultrathin black phosphorus devices. Nano Lett, 2017, 17: 5361–5367

135 Wu Q, Shen L, Bai Z, et al. Efficient spin injection into graphene through a tunnel barrier: overcoming the spin-conductance mismatch. Phys Rev Appl, 2014, 2: 044008

136 Liang Y, Zhu J, Xiao F, et al. Nanoscale inverters enabled by a facile dry-transfer technique capable of fast prototyping of emerging two-dimensional electronic devices. In: Proceedings of the 5th IEEE Electron Devices Technology and Manufacturing Conference (EDTM), 2021. 1–3

137 Fei Z, Zhao W, Palomaki T A, et al. Ferroelectric switching of a two-dimensional metal. Nature, 2018, 560: 336–339

138 dos Santos J M B L, Peres N M R, Neto A H C. Graphene bilayer with a twist: electronic structure. Phys Rev Lett, 2007, 99: 256802

139 Cao Y, Luo J Y, Fatemi V, et al. Superlattice-induced insulating states and valley-protected orbits in twisted bilayer graphene. Phys Rev Lett, 2016, 117: 116804

140 Kim K, DaSilva A, Huang S, et al. Tunable Moiré bands and strong correlations in small-twist-angle bilayer graphene. Proc Natl Acad Sci USA, 2017, 114: 3364–3369

141 Yasuda K, Wang X, Watanabe K, et al. Stacking-engineered ferroelectricity in bilayer boron nitride. Science, 2021, 372: 1458–1462

142 Liu X, Wang W, Yang F, et al. Bi_2O_2Se/BP van der Waals heterojunction for high performance broadband photodetector. Sci China Inf Sci, 2021, 64: 140404

143 Wu S, Wang X, Jiang W, et al. Interface engineering of ferroelectric-gated MoS_2 phototransistor. Sci China Inf Sci, 2021, 64: 140407

144 Shen P C, Su C, Lin Y, et al. Ultralow contact resistance between semimetal and monolayer semiconductors. Nature, 2021, 593: 211–217

145 Dang Z, Wang W, Chen J, et al. Vis-NIR photodetector with microsecond response enabled by 2D bismuth/Si(111) heterojunction. 2D Mater, 2021, 8: 035002

146 Meng W, Xu F, Yu Z, et al. Three-dimensional monolithic micro-LED display driven by atomically thin transistor matrix. Nat Nanotechnol, 2021, 16: 1231–1236

147 Huang M, Li S, Zhang Z, et al. Multifunctional high-performance van der Waals heterostructures. Nat Nanotechnol, 2017, 12: 1148–1154

148 Xiong X, Kang J, Hu Q, et al. Reconfigurable logic-in-memory and multilingual artificial synapses based on 2D heterostructures. Adv Funct Mater, 2020, 30: 1909645

149 Shih C C, Huang M H, Wan C K, et al. Tuning interface barrier in 2D BP/$ReSe_2$ heterojunctions in control of optoelectronic performances and energy conversion efficiencies. ACS Photon, 2020, 7: 2886–2895

150 Li D, Chen M, Sun Z, et al. Two-dimensional non-volatile programmable p-n junctions. Nat Nanotechnol, 2017, 12: 901–906

151 Mukherjee B, Zulkefli A, Watanabe K, et al. Laser-assisted multilevel non-volatile memory device based on 2D van-der-Waals few-layer-ReS_2/h-BN/graphene heterostructures. Adv Funct Mater, 2020, 30: 2001688

152 Mukherjee B, Hayakawa R, Watanabe K, et al. ReS_2/h-BN/graphene heterostructure based multifunctional devices: tunneling diodes, FETs, logic gates, and memory. Adv Electron Mater, 2021, 7: 2000925

153 Wang B, Luo H, Wang X, et al. Bifunctional NbS_2-based asymmetric heterostructure for lateral and vertical electronic devices. ACS Nano, 2020, 14: 175–184

154 Hu R, Wu E, Xie Y, et al. Multifunctional anti-ambipolar p-n junction based on $MoTe_2$/MoS_2 heterostructure. Appl Phys Lett, 2019, 115: 073104

155 Lee J, Duong N T, Bang S, et al. Modulation of junction modes in $SnSe_2$/$MoTe_2$ broken-gap van der Waals heterostructure for multifunctional devices. Nano Lett, 2020, 20: 2370–2377

156 Afzal A M, Iqbal M Z, Dastgeer G, et al. Highly sensitive, ultrafast, and broadband photo-detecting field-effect transistor with transition-metal dichalcogenide van der Waals heterostructures of $MoTe_2$ and $PdSe_2$. Adv Sci, 2021, 8: 2003713

157 Datta K, Shadman A, Rahman E, et al. Trilayer TMDC heterostructures for MOSFETs and nanobiosensors. J Electron Mater, 2017, 46: 1248–1260

158 Vu Q A, Shin Y S, Kim Y R, et al. Two-terminal floating-gate memory with van der Waals heterostructures for ultrahigh on/off ratio. Nat Commun, 2016, 7: 12725

159 Sundararaju U, Haniff M A S M, Ker P J, et al. MoS_2/h-BN/graphene heterostructure and plasmonic effect for self-powering photodetector: a review. Materials, 2021, 14: 1672

160 He J, Fang N, Nakamura K, et al. 2D tunnel field effect transistors (FETs) with a stable charge-transfer-type p^+-WSe_2 source. Adv Electron Mater, 2018, 4: 1800207

161 Balaji Y, Smets Q, Śabo Á, et al. MoS_2/$MoTe_2$ heterostructure tunnel FETs using gated Schottky contacts. Adv Funct Mater, 2020, 30: 1905970

162 Fiori G, Betti A, Bruzzone S, et al. Lateral graphene-hBCN heterostructures as a platform for fully two-dimensional transistors. ACS Nano, 2012, 6: 2642–2648

163 Tang H L, Chiu M H, Tseng C C, et al. Multilayer graphene-WSe_2 heterostructures for WSe_2 transistors. ACS Nano, 2017, 11: 12817–12823

164 Yang Z, Pan J, Liu Q, et al. Electronic structures and transport properties of a MoS_2-NbS_2 nanoribbon lateral heterostructure. Phys Chem Chem Phys, 2017, 19: 1303–1310

165 Liu Q, Ouyang F, Yang Z, et al. Electronic properties and transistors of the NbS_2-MoS_2-NbS_2 NR heterostructure. Nanotechnology, 2017, 28: 075702

166 Lee G H, Yu Y J, Cui X, et al. Flexible and transparent MoS_2 field-effect transistors on hexagonal boron nitride-graphene heterostructures. ACS Nano, 2013, 7: 7931–7936

167 Shih C J, Wang Q H, Son Y, et al. Tuning on-off current ratio and field-effect mobility in a MoS_2-graphene heterostructure via Schottky barrier modulation. ACS Nano, 2014, 8: 5790–5798

168 Moriya R, Yamaguchi T, Inoue Y, et al. Large current modulation in exfoliated-graphene/MoS_2/metal vertical heterostructures. Appl Phys Lett, 2014, 105: 083119

169 Sata Y, Moriya R, Yamaguchi T, et al. Modulation of Schottky barrier height in graphene/MoS_2/metal vertical heterostructure with large current ON-OFF ratio. Jpn J Appl Phys, 2015, 54: 04DJ04

170 Tran M D, Kim H, Kim J S, et al. Two-terminal multibit optical memory via van der Waals heterostructure. Adv Mater, 2019, 31: 1807075

171 Oliva N, Backman J, Capua L, et al. WSe_2/$SnSe_2$ vdW heterojunction tunnel FET with subthermionic characteristic and MOSFET co-integrated on same WSe_2 flake. npj 2D Mater Appl, 2020, 4: 5

172 Liu H, Hussain S, Ali A, et al. A vertical WSe_2-$MoSe_2$ p-n heterostructure with tunable gate rectification. RSC Adv, 2018, 8: 25514–25518

173 Yi J, Sun X, Zhu C, et al. Double-gate MoS_2 field-effect transistors with full-range tunable threshold voltage for multifunctional logic circuits. Adv Mater, 2021, 33: 2101036

174 Wang F, Yin L, Wang Z, et al. Strong electrically tunable $MoTe_2$/graphene van der Waals heterostructures for high-performance electronic and optoelectronic devices. Appl Phys Lett, 2016, 109: 193111

175 Yang Z, Kim C, Lee K Y, et al. A Fermi-level-pinning-free 1D electrical contact at the intrinsic 2D MoS$_2$-metal junction. Adv Mater, 2019, 31: 1808231

176 Lee J, Parrish K N, Chowdhury S F, et al. State-of-the-art graphene transistors on hexagonal boron nitride, high-k, and polymeric films for GHz flexible analog nanoelectronics. In: Proceedings of International Electron Devices Meeting, 2012

177 Lee J, Tao L, Parrish K N, et al. Multi-finger flexible graphene field effect transistors with high bendability. Appl Phys Lett, 2012, 101: 252109

178 Yao H, Wu E, Liu J. Frequency doubler based on a single MoTe$_2$/MoS$_2$ anti-ambipolar heterostructure. Appl Phys Lett, 2020, 117: 123103

179 Yuan L, Chung T F, Kuc A, et al. Photocarrier generation from interlayer charge-transfer transitions in WS$_2$-graphene heterostructures. Sci Adv, 2018, 4: e1700324

180 Liu Y, Liu C, Wang X, et al. Photoresponsivity of an all-semimetal heterostructure based on graphene and WTe$_2$. Sci Rep, 2018, 8: 12840

181 Chen Y, Wang Y, Wang Z, et al. Unipolar barrier photodetectors based on van der Waals heterostructures. Nat Electron, 2021, 4: 357–363

182 Long M, Liu E, Wang P, et al. Broadband photovoltaic detectors based on an atomically thin heterostructure. Nano Lett, 2016, 16: 2254–2259

183 Wu W, Zhang Q, Zhou X, et al. Self-powered photovoltaic photodetector established on lateral monolayer MoS$_2$-WS$_2$ heterostructures. Nano Energy, 2018, 51: 45–53

184 Britnell L, Ribeiro R M, Eckmann A, et al. Strong light-matter interactions in heterostructures of atomically thin films. Science, 2013, 340: 1311–1314

185 Hu S, Xu J, Zhao Q, et al. Gate-switchable photovoltaic effect in BP/MoTe$_2$ van der Waals heterojunctions for self-driven logic optoelectronics. Adv Opt Mater, 2021, 9: 2001802

186 Yu W J, Liu Y, Zhou H, et al. Highly efficient gate-tunable photocurrent generation in vertical heterostructures of layered materials. Nat Nanotechnol, 2013, 8: 952–958

187 Furchi M M, Pospischil A, Libisch F, et al. Photovoltaic effect in an electrically tunable van der Waals heterojunction. Nano Lett, 2014, 14: 4785–4791

188 Murthy A A, Stanev T K, Cain J D, et al. Intrinsic transport in 2D heterostructures mediated through h-BN tunneling contacts. Nano Lett, 2018, 18: 2990–2998

189 Zhou Y, Xu W, Sheng Y, et al. Symmetry-controlled reversible photovoltaic current flow in ultrathin all 2D vertically stacked graphene/MoS$_2$/WS$_2$/graphene devices. ACS Appl Mater Interf, 2019, 11: 2234–2242

190 Hou L, Zhang Q, Tweedie M, et al. Photocurrent direction control and increased photovoltaic effects in all-2D ultrathin vertical heterostructures using asymmetric h-BN tunneling barriers. ACS Appl Mater Interf, 2019, 11: 40274–40282

191 Furchi M M, Höller F, Dobusch L, et al. Device physics of van der Waals heterojunction solar cells. npj 2D Mater Appl, 2018, 2: 3

192 Linghu J, Yang T, Luo Y, et al. High-throughput computational screening of vertical 2D van der Waals heterostructures for high-efficiency excitonic solar cells. ACS Appl Mater Interf, 2018, 10: 32142–32150

193 Kar M, Sarkar R, Pal S, et al. Tunable electronic structure of two-dimensional MoX$_2$ (X = S, Se)/SnS$_2$ van der Waals heterostructures. J Phys Chem C, 2020, 124: 21357–21365

194 Rahman M S, Anower M S, Abdulrazak L F. Utilization of a phosphorene-graphene/TMDC heterostructure in a surface plasmon resonance-based fiber optic biosensor. Photon Nanostruct Fund Appl, 2019, 35: 100711

195 Wu L, Guo J, Wang Q, et al. Sensitivity enhancement by using few-layer black phosphorus-graphene/TMDCs heterostructure in surface plasmon resonance biochemical sensor. Sensors Actuat B-Chem, 2017, 249: 542–548

196 Zheng G, Zou X, Chen Y, et al. Fano resonance in graphene-MoS$_2$ heterostructure-based surface plasmon resonance biosensor and its potential applications. Opt Mater, 2017, 66: 171–178

197 Rahman M M, Rana M M, Rahman M S, et al. Sensitivity enhancement of SPR biosensors employing heterostructure of PtSe$_2$ and 2D materials. Opt Mater, 2020, 107: 110123

198 Loan P T K, Zhang W, Lin C T, et al. Graphene/MoS$_2$ heterostructures for ultrasensitive detection of DNA hybridisation. Adv Mater, 2014, 26: 4838–4844

199 Li N, Tang T, Li J, et al. Highly sensitive biosensor with graphene-MoS$_2$ heterostructure based on photonic spin Hall effect. J Magn Magn Mater, 2019, 484: 445–450

200 Li F, Wang S, Yin H, et al. Photoelectrochemical biosensor for DNA formylation detection in genomic DNA of maize seedlings based on black TiO$_2$-enhanced photoactivity of MoS$_2$/WS$_2$ heterojunction. ACS Sens, 2020, 5: 1092–1101

201 Choi C, Choi M K, Liu S, et al. Human eye-inspired soft optoelectronic device using high-density MoS$_2$-graphene curved image sensor array. Nat Commun, 2017, 8: 1664

202 Ghobadi N, Pourfath M. Vertical tunneling graphene heterostructure-based transistor for pressure sensing. IEEE Electron Device Lett, 2015, 36: 280–282

203 Chhetry A, Sharma S, Barman S C, et al. Black phosphorus@laser-engraved graphene heterostructure-based temperature-strain hybridized sensor for electronic-skin applications. Adv Funct Mater, 2021, 31: 2007661

204 Phan D T, Park I, Park A R, et al. Black P/graphene hybrid: a fast response humidity sensor with good reversibility and stability. Sci Rep, 2017, 7: 10561

205 Cho B, Yoon J, Lim S K, et al. Chemical sensing of 2D graphene/MoS$_2$ heterostructure device. ACS Appl Mater Interf, 2015, 7: 16775–16780

206 Tabata H, Sato Y, Oi K, et al. Bias- and gate-tunable gas sensor response originating from modulation in the Schottky barrier height of a graphene/MoS$_2$ van der Waals heterojunction. ACS Appl Mater Interf, 2018, 10: 38387–38393

207 Hong H S, Phuong N H, Huong N T, et al. Highly sensitive and low detection limit of resistive NO$_2$ gas sensor based on a MoS$_2$/graphene two-dimensional heterostructures. Appl Surface Sci, 2019, 492: 449–454

208 Pham T, Ramnani P, Villarreal C C, et al. MoS$_2$-graphene heterostructures as efficient organic compounds sensing 2D

materials. Carbon, 2019, 142: 504–512

209 Ikram M, Liu L, Liu Y, et al. Fabrication and characterization of a high-surface area MoS_2@WS_2 heterojunction for the ultra-sensitive NO_2 detection at room temperature. J Mater Chem A, 2019, 7: 14602–14612

210 Kim Y, Lee S, Song J G, et al. 2D Transition metal dichalcogenide heterostructures for p- and n-type photovoltaic self-powered gas sensor. Adv Funct Mater, 2020, 30: 2003360

211 Liu C, Yan X, Song X, et al. A semi-floating gate memory based on van der Waals heterostructures for quasi-non-volatile applications. Nat Nanotechnol, 2018, 13: 404–410

212 Li D, Wang X, Zhang Q, et al. Nonvolatile floating-gate memories based on stacked black phosphorus-boron nitride-MoS_2 heterostructures. Adv Funct Mater, 2015, 25: 7360–7365

213 Liu C, Zou X, Wu M C, et al. Polarization-resolved broadband MoS_2/black phosphorus/MoS_2 optoelectronic memory with ultralong retention time and ultrahigh switching ratio. Adv Funct Mater, 2021, 31: 2100781

214 Bertolazzi S, Krasnozhon D, Kis A. Nonvolatile memory cells based on MoS_2/graphene heterostructures. ACS Nano, 2013, 7: 3246–3252

215 Liu L, Liu C, Jiang L, et al. Ultrafast non-volatile flash memory based on van der Waals heterostructures. Nat Nanotechnol, 2021, 16: 874–881

216 Ye F, Lee J, Feng P X L. Atomic layer MoS_2-graphene van der Waals heterostructure nanomechanical resonators. Nanoscale, 2017, 9: 18208–18215

217 Kumar R, Session D W, Tsuchikawa R, et al. Circular electromechanical resonators based on hexagonal-boron nitride-graphene heterostructures. Appl Phys Lett, 2020, 117: 183103

218 Kim S P, Yu J, van der Zande A M. Nano-electromechanical drumhead resonators from two-dimensional material bimorphs. Nano Lett, 2018, 18: 6686–6695

219 Ye F, Islam A, Zhang T, et al. Ultrawide frequency tuning of atomic layer van der Waals heterostructure electromechanical resonators. Nano Lett, 2021, 21: 5508–5515